6G BRAINS Deliverable D3.4

Hybrid Deterministic/Stochastic Raytracing based Channel Model for Multiband Analysis in Industry Scenario

Editor:	Diego Dupleich (FhG)
Deliverable nature:	Report (R)
Dissemination level: (Confidentiality)	Public (PU)
Contractual delivery date:	30 April 2023
Actual delivery date:	16 October 2023
Suggested readers:	Consortium members, reviewers, researchers
Version:	1.0
Total number of pages:	55
Keywords:	Point cloud, raytracing, multi-band propagation measurements, channel modelling, Industry 4.0

Abstract

The present report introduces the results on channel modelling at sub-6 GHz, mmWave, and sub-THz in the industrial scenarios discussed in 6G BRAINS. This model is a quasi-deterministic approach based on raytracing (RT) simulations from precise maps obtained from 3D laser scans plus stochastic components derived from extensive radiofrequency (RF) measurements in the same scenarios. The laser and RF measurements were conducted in a Bosch factory and a machine room in the facilities of FhG, both in Germany. The acquisition of the 3D CAD models was discussed in Deliverable D3.1, the RF measurement results in Deliverable D3.3, and in the present deliverable we validate the RT model by direct comparison between the simulations and measurements, while introducing the stochastic parameters extracted from the RF measurements. This raytracing model allows simulations with spatial consistency over the different bands of interest in 6G BRAINS, providing an accurate geometrical representation of the environment from the propagation properties for precise localization applications.

Disclaimer

This document contains material, which is the copyright of certain 6G BRAINS consortium parties and may not be reproduced or copied without permission.

In case of Public (PU):

All 6G BRAINS consortium parties have agreed to full publication of this document.

In case of Restricted to Programme (PP):

All 6G BRAINS consortium parties have agreed to make this document available on request to other framework program participants.

In case of Restricted to Group (RE):

All 6G BRAINS consortium parties have agreed to full publication of this document. However, this document is written for being used by <organisation / other project / company etc.> as <a contribution to standardisation / material for consideration in product development etc.>.

In case of Consortium confidential (CO):

The information contained in this document is the proprietary confidential information of the 6G BRAINS consortium and may not be disclosed except in accordance with the consortium agreement.

The commercial use of any information contained in this document may require a license from the proprietor of that information.

Neither the 6G BRAINS consortium as a whole, nor a certain part of the 6G BRAINS consortium warrant that the information contained in this document is capable of use, nor that use of the information is free from risk, accepting no liability for loss or damage suffered by any person using this information.

The EC flag in this document is owned by the European Commission and the 5G PPP logo is owned by the 5G PPP initiative. The use of the EC flag and the 5G PPP logo reflects that 6G BRAINS receives funding from the European Commission, integrated in its 5G PPP initiative. Apart from this, the European Commission and the 5G PPP initiative have no responsibility for the content of this document.

Impressum

[Full project title]	Bring Reinforcement-learning Into Radio Light Network for Massive Connections
[Short project title]	6G BRAINS
[Number and title of work-package]	WP3: 6G Physical Propagation Measurements and Modelling, from Microwave to THz and OWC
[Number and title of task]	T3.1: Multi-Band (MW + mmWave + THz + OWC) Channel Measurements in the Industrial Network Environments and Industrial Applications
	T3.2: Analysis of measurement data and elaboration of the differences in wave propagation
	T3.3: Common fused channel model for the industrial network environments and industrial
[Document title]	Hybrid deterministic/stochastic raytracing-based channel model for multiband analysis in industry scenario
[Editor: Name, company]	Diego Dupleich, FhG
[Work-package leader: Name, company]	Diego Dupleich, FhG
[Estimation of PM spent on the Deliverable]	30

Executive summary

6G BRAINS envisions the integration of novel spectrum bands to support the development of ubiquitous smart wireless communications in industrial scenarios. Future industrial tasks and services rely on the simultaneous utilization of sub-6 GHz, mm-waves, THz, and optical wireless communications (OWC). The free blocks of spectrum available at THz and OWC enables the implementation of innovatively high data rate wireless links with enhanced capacity, reliability, and latency. Furthermore, THz and OWC allow resolution on 3D simultaneous localization and mapping (SLAM) of up to 1 mm accuracy. Therefore, reliable channel models based on empirical evidence addressing these frequencies are of exceptional importance for the design, performance evaluation, standardization, and deployment of the future 6G networks.

However, the development and parametrization of a single model covering such a wide spectrum of frequency bands and applications is challenging in multiple aspects. Localization and imaging applications require a precise correspondence between the geometrical properties of the propagated paths and the location of users and scatterers. Moreover, testing heterogeneous localization methods, based on the combination of localization methods in different bands, requires spatial consistency of the model not only in the spatial domain, but also in the frequency domain: the scatterers must be in the same position for the different simulated bands. While the 3GPP 38.901 spatial model covers from 0.5 GHz to 100 GHz [3GP20], the stochastic approach on the modelling of scatterers limits the usability of these models in these scenarios. Therefore, models with deterministic component are more appropriate for these applications.

Depending on the parametrization and diversity of the constructive materials in the map, raytracing (RT) tools allow simultaneous simulations at different frequencies with a precise geometrical representation of the environment in the propagation parameters of the paths. Nonetheless, the comparability of the results with reality depends on the complexity of the RT map/model. Thus, obtaining an accurate RT model with a high level of details and large number of objects is of crucial importance.

Therefore, one of the goals of the WP3 in 6G BRAINS is to obtain a precise multi-band fused channel model for simultaneous RF and OWC simulations. This model allows both very precise and accurate RT results from real scenarios (maps from 3D laser scans) of interest withing 6G BRAINS, and/or statistical results from the generalization of these scenarios for statistical analysis. This model consists of a deterministic part from precise RT simulations of accurate maps and a stochastic part, consisting of components whose properties are either deterministically or purely stochastically calculated.

List of authors

Company	Author	Contribution
Fraunhofer IIS	Diego Dupleich	Section 1 to 7
Fraunhofer IIS	Han Niu	Section 4.3.1
Fraunhofer IIS	Yanneck Völker-Schöneberg	Section 3.1
Oledcomm	Bastien Béchadergue	Section 2.2
ISEP	Xun Zhang	Section 3.2 and Section 6
ISEP	Xiadong Liu	Section 3.2 and Section 6

Table of Content

List of figures and tables

Abbreviations

3GPP	3rd Generation Partnership Project
5G	Fifth Generation (mobile/cellular networks)
5G PPP	5G Infrastructure Public Private Partnership
6G BRAINS	Bringing Reinforcement learning Into Radio Light Network for Massive Connections
AMC	Adaptive Modulation and Coding
AP	Access Point
ASA	Azimuth Spread of Arrival
ASD	Azimuth Spread of Departure
BS	Base Station
CAD	Computer-aided Design
CQI	Channel Quality Index
DMC	Dense Multipath Component
DoA	Direction of Arrival
DoD	Direction of Departure
DS	Delay Spread
GO	Geometrical Optics
GTD	Geometrical Theory of Diffraction
GTP	Geometrical Theory of Propagation
IAB	Integrated Access and Backhaul
ISAC	Integrated Sensing and Communication
IoT	Internet of Things
KPI	Key Performance Indicator
LSP	Large Scale Parameter
M2M	Machine to Machine

MLBS	Maximum Length Binary Sequence
MPC	Multi-Path Component
PDP	Power Delay Profile
RT	Raytracing
RX	Receiver
SCM	Spatial Channel Model
SISO	Single Input Single Output
SLAM	Simultaneous Localization and Mapping
ToF	Time of Flight
UE	User Equipment
mUE	Mobile User Equipment
SCM	Spatial Channel Model
SINR	Signal-to-Interference-Plus-Noise Ratio
SNR	Signal-to-Noise Ratio
TX	Transmitter
WP3	Work Package Three

1   Introduction

Channel models are key enablers for the design and development of communication systems, allowing the prediction of the channel in different situations for testing the response of systems and algorithms.

The main challenge within the applications foreseen in 6G BRAINS is to obtain a single channel model with the capabilities to cover all the testing requirements:

- Multi-band simulations addressing RF and OWC technologies: base stations (BS) or access point (AP) and user equipment (UE) might operate simultaneously with multiple radio interfaces at different frequencies. Therefore, the model must provide a frequency dependent channel impulse response (CIR).
- Correlation over the different bands given by the geometrical properties of the location of the scatterers: this enables simulations to test inter-band algorithms, as assisted beamforming, or heterogeneous multiband localization methods, in which certain properties related to the position of the user can be estimated at lower frequencies, and then, the large available bandwidths at higher frequencies can be used to increase the accuracy.
- Realistic in terms of the geometrical description of the environment from the delay and angular propagation properties. Applications as imaging and localization rely on the geometrical properties of the scattered paths.

The complexity of the models depends on the properties of the systems and the parameters under test. For example, for a SISO system under test whose evaluation parameter is coverage or received signal-to-noise ratio (SNR), empirical path-loss models offer an efficient trade-off between complexity and accuracy. Fading models based on statistics are sufficient for narrowband systems without the capability of resolving MPCs in the delay domain.

On the other hand, when the resolution of the systems increases in a certain domain, the spreading characteristics of the signals become a relevant parameter. For example, a key parameter on the design of broad and wideband systems is the information of the spreading in the delay domain, i.e., delay spread. Similar is the case for the spatial domain. At high frequencies, high gain or multi-antenna systems usually employ hybrid beamformers in which the analogue component steers the array gain in the direction of the dominant paths to compensate the isotropic path-loss. Therefore, the geometrical properties of the environment, and propagation parameters as time of flight (ToF), direction of arrival (DoA), and direction of departure (DoD) become fundamental in these models. The accuracy of these parameters also defines the applicability of the model for different applications.

In addition, aspects as spatial consistency become more relevant when mobile systems under test requires the knowledge of the location of the scatterers during displacement, for example, if they need to consistently track the source of scattered signal to re-point the gain of the antennas. Moreover, applications as SLAM need an accurate description of the simulated environment to test realistic conditions.

Physical channel models are frequently classified as deterministic or stochastic. The former ones are characterized by offering the same channel realization in every run, and the latter generates different realizations of the channel in every execution, since the parameters are based on statistical distributions. A third type of classification that is currently gaining relevance for physical channel models for high frequency applications are the hybrid

deterministic/stochastic models. These models combine deterministic and stochastic components to address different features of the channel [MET15], [WPK16]. Usually, the deterministic part is based on simplified geometrical calculations [PJK11] or RT maps with certain complexity, and the stochastic is derived from statistics obtained from extensive measurement campaigns.

RT is a deterministic methodology for propagation modelling based on the geometrical theory of propagation (GTP). GTP is an extension of geometrical optics (GO) including geometrical theory of diffraction (GTD). GTP is based on the concepts of rays to treat the different propagation mechanisms: reflection and transmission on plane surfaces and diffraction on edges. The main assumptions in RT are far-field (electromagnetic waves are considered as plane waves) and high frequency (the wavelength is small compared to the objects in the environment). In addition, different methods can also be incorporated to treat diffuse scattering in RT [DFV07]. RT models are based on 2D or 3D maps of the environment. The level of details in the environment adds complexity to the simulations and accuracy to the results. The complexity of the maps depends on the efforts expended during its the acquisition. However, this effort is minimized with the available technology on point cloud laser scanners compared to a handcrafted map.

Moreover, RT is suitable for multiband simulations. If the map is parametrized with the electromagnetic properties of the constructive materials at different frequencies, the simulations of links operating simultaneously in different bands are therefore straightforward.

However, RT alone is not able to capture multiple propagation characteristics, mostly due to the limited amount of computing time and resources. The limited number of rays and interactions order that are possible to calculate (depending also on the level of details and size of the map) limits aspects as diffuse scattering and dense multipath components (DMC). In that regard, RT simulations can be enriched with the addition of components from stochastic distributions, more specifically for components that cannot be resolved by the system.

Therefore, given the requirements listed before for the physical channel model within 6G BRAINS, the hybrid deterministic/stochastic methodology offers a good compromise between accuracy and complexity.

A simple workflow of the process described in this document is shown in Figure 1 and the details for each step are addressed in the following sections.
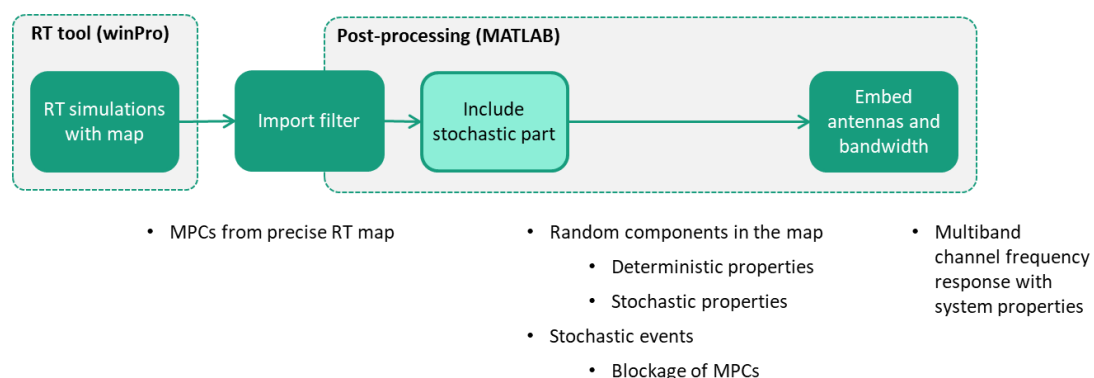
Figure 1: Channel synthesis workflow with stochastic/deterministic components and system aspects.

In this document, we focus on the description and validation with measurements of a hybrid deterministic/stochastic channel model. This model can be used in two different ways: as a pure standalone deterministic model with a very precise map of the environments studied in 6G BRAINS, or as the baseline model integrating stochastic components. While the complete modelling methodology is described in this document, only part of them have been parametrized from measurements within 6G BRAINS. Other components were obtained from previous results found in the literature, and other components are left for future work.

1.1   Objective of this Document

The main objectives of this document can be summarized as follows:

- Summarizing the state of the art in multiband physical channel models for RF and OWC
- Introducing the methodology adopted in WP3 in 6G BRAINS for multiband propagation simulations.
- Introducing a new RT map from 3D point-cloud scans to increase the diversity of scenarios within 6G BRAINS for industrial applications, following a similar approach as the one described in Deliverable 3.1.
- Validating the channel model with measurements

1.2   Relation to other Deliverables within the WP3

This deliverable D3.4 introduces the modelling methodology used for the multiband physical channel model developed in the WP3 of the 6G BRAINS project.

The Figure 2 presents the relation between the workflow of the WP3 and the different deliverables within the WP3. The process of obtaining the RT map from point-cloud data was described in D3.1, where the model of the industrial hall from Bosch at Blaichach was introduced. The deliverable D3.2 summarizes the integration of the different technologies for quad-band channel measurements at RF and OWC, as well as the different calibration methodologies and test measurements. The results and analysis of these measurements are presented in Deliverable D3.3. These results are then used in the deliverable D3.4 to validate the maps and modelling methodology adopted for the physical channel model presented in WP3.

The verification of the RT simulations based on RF and OWC measurements is divided into two aspects: the verification of the map by identifying differences between the geometrical properties obtained from the measured propagation paths and the geometry of the scenario, and the verification of the electromagnetic properties of the assigned materials to the RT model by comparing the amplitude levels of the different paths identified in the measurements. Finally, once the RT model is verified and calibrated, stochastic components obtained from the measurements are incorporated to the RT results to obtain the fused multi-band channel model for industrial scenarios.

Deliverable D3.5 finally addresses the results based on the integration of other physical layer aspects as waveforms.
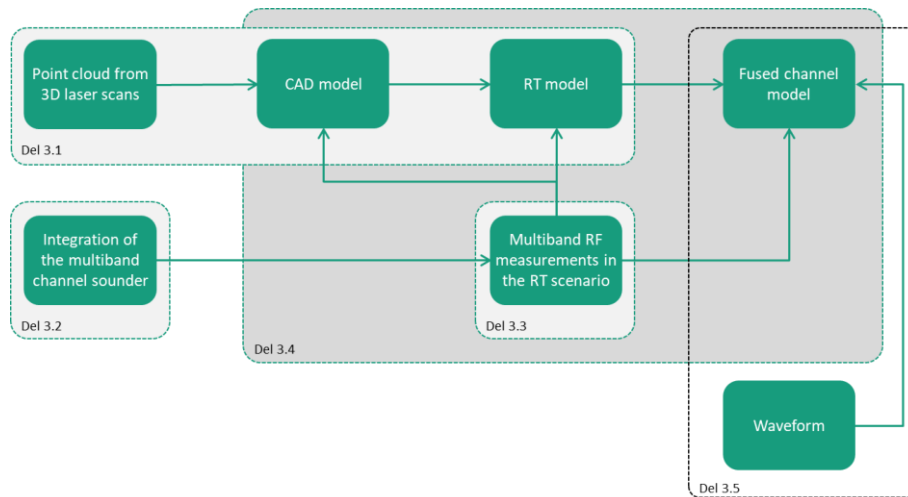
Figure 2: Relation between workflow of the WP3 and the deliverables.

1.3 Structure of this Document

The rest of the document is organized as follows: in Section 2 we introduce and overview of hybrid deterministic/stochastic channel models. In addition, we present the concept of the multiband channel model and the interface to other work packages within 6G BRAINS. In Section 3 we introduce a new scenario where the measurements were conducted for parametrization of the model. In Section 4 we introduce the modelling approach behind the hybrid/stochastic 6G BRAINS physical model. Finally, in Section 5 we compare the RT model of the machine room scenario with multi-band RF measurements for validation of the results. Similarly, the laboratory model is validated with OWC measurements in Section 6. A conclusion is finally summarized with future tasks in Section 7.

2   Overview of Channel Models

2.1   Stochastic and Deterministic Physical RF Channel Models

Physical models can be sub-classified into deterministic or stochastic. The main difference is that while the former ones provide the same result every time they are executed, the latter ones generate a different channel realization on every run since the output is randomly drawn from statistic distributions. This feature allows the test of wireless systems under different channels and conditions. Therefore, it is also usual that while the deterministic models are used to analyse specific features under controlled circumstances and for planning, the results obtained with stochastic models are based on the analysis of statistics which allows a wider generalization.

The stochastic or deterministic term is applied here to the nature of the model itself, and not to the components inside of the model since stochastic models can also have deterministic components inside. Examples are the map-based models in METIS [MET15], the quasi-deterministic models in MiWEBA [WPK16], and the inclusion of explicit components as ground reflection within the 3GPP SCM family [3GP20]. However, all these simulators produce a different channel every time they are run. Similarly, components or aspects as shadowing can be treated in some models deterministically (e.g., with the double edge-knife diffraction approach in METIS) or stochastically, as in MiWEBA.

RT is an example of deterministic models. The simulated channel in these cases account with more realistic characteristics and considers detailed physic processes. RT offers a very accurate prediction of the propagation at expenses of high computational needs. However, the accuracy of the results highly depends on the level of details used to describe the scenario, i.e., amount and shape of objects and their electromagnetic properties. The high complexity and computation costs, together with the site and scenario specificity, limits the applicability of deterministic models. On the other hand, physical stochastic models are pertinent for the generalization of results. They don't necessarily represent a realistic case in a single realization, but the ensemble statistics of multiple repetitions fit with the statistics of real scenarios. Thus, stochastic models don't relate the propagation parameters of the MPCs to particular scatterers, but the parameters are drawn from multi-dimensional random processes, whose distributions are obtained from extensive measurement campaigns. This means that the CIR doesn't correspond to a particular propagation environment, but its statistics do, providing realistic propagation properties to imaginary scatterers. In contrast to deterministic models, physical stochastic models offer high flexibility of generating CIRs for multiple scenarios, being much lighter in terms of computation, but at expenses of reduced accuracy. Examples of stochastic models are the WIN-II [12], the 3GPP SCM [3GP20], COST 2100 [13], METIS [MET15], and MiWEBA [WPK16], between others.

The following figure intends to summarize graphically (simplified) the level of deterministic and stochastic nature of the different models, showing the aim of the 6G BRAINS Channel Model in this regard.

Stochastic				WINNER II, 3GPP
Deterministic	Stochastic			COST 2100, Stochastic METIS
Deterministic		Stochastic		MIWEBA
Deterministic			Stochastic	Map-based METIS, 6G BRAINS
Deterministic				RT
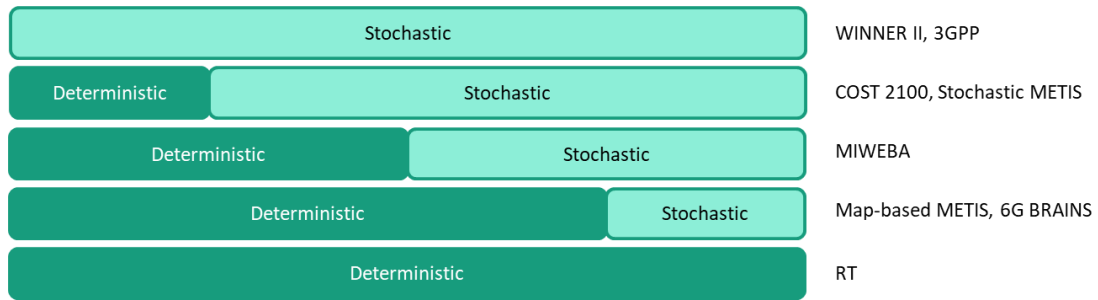
Figure 3: Stochastic vs deterministic models.

2.2 OWC Channel Models

Many models of the OWC channel have been proposed in the literature, as illustrated by the typology of Al-Kinani *et al.* [AWZ18], shown in Figure 4. These modelling methods can be divided into two main categories - deterministic methods and stochastic methods - which gather themselves several approaches.
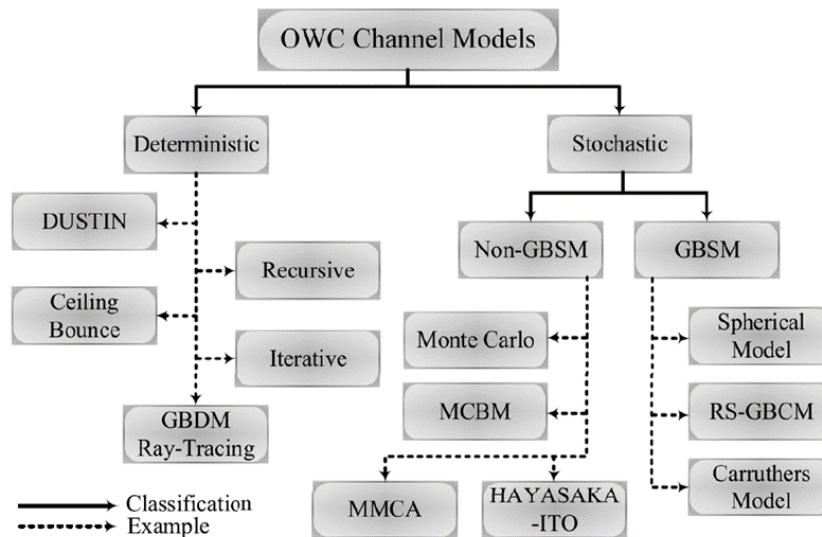
Figure 4: OWC channel models classification (extracted from [AWZ18]).

2.2.1 Deterministic Methods

Among deterministic methods, the oldest technique was proposed by Gfeller and Bapst in 1979 [GB79]. They were inspired by the radiosity method, from the field of image synthesis, to simulate the impulse response of the OWC channel. However, this approach only dealt with a single reflection, so it was later extended by Barry *et al.* for multiple successive reflections [BKK93]. In this work, each surface of the environment is modelled as a set of elementary surfaces acting as purely Lambertian reflectors, with a fixed reflection coefficient. To evaluate the impulse response of the channel, the contribution of each reflector is added to the power received at the receiver, if the latter is in visibility of the reflector, as well as to the power received by the other reflectors in line of sight for reflections of order greater than one.

In practice, the contribution of these higher order reflections can be computed recursively, as in Barry *et al.* [BKK93] and more efficiently in other subsequent works [KB97], [LPB11], or

iteratively, as proposed by Carruthers & Kannan [CK02]. However, these two approaches suffer from the same limitations. Besides the fact that they only work for purely diffuse surfaces, their efficient implementation remains complex. Moreover, they introduce a bias in the estimation of the impulse response due to the discretization of the surfaces of the environment, which can only be reduced by drastically decreasing the size of the reflectors and thus considerably increasing the computation time and the memory required for their realization.

For these reasons, iterative and recursive methods are poorly suited to handle complex environments, especially when considering third order reflections and above, despite optimizations such as those proposed in the DUSTIN algorithm [LHB97]. A nevertheless promising approach, recently developed by Schulze, consists in transposing the radiosity method to the frequency domain, which allows to considerably decrease the computational time while considering an infinite number of reflections. However, its use is still limited to the case of purely diffuse surfaces (Lambertian), and the manual definition of the environment (e.g., reflectors position and characteristics) remains very laborious [SCH16]. To overcome the latter issue, LIDAR-assisted environment modelling has recently been proposed in [MGK22]. A Leica RTC 360 scanner is used to capture a 3D point cloud of the environment, which is then pre-processed to assign reflectance parameters to the different walls and objects. The frequency-domain approach proposed by Schulze is finally applied to estimate the channel impulse response including all-order reflections.

The ceiling-bounce model, first proposed by Carruthers & Kahn in 1997 [CK97] and then taken up and improved in several works [PBB97; AJ07; CBH16], consists in modelling the impulse response of the OWC channel by considering only one reflection, from the respective distances between the receivers and the reflecting surface as well as a parameter related to the dispersion of the channel delays. It is therefore based on a coarse environment model and on very simple analytical formulas, which makes it an easy and fast method, but at the expense of its accuracy, especially in complex environments.

On the other hand, the complexity of the environment is particularly well taken into account by geometry-based deterministic models (GBDM) based on raytracing (RT). These methods are based on the modelling, for example with CAD software, of the OWC environment, then on the RT simulation of all the rays ending their course at a given receiver point. For this, commercial software such as OpticsStudio has been used in several works [SUA14; MU15; YH22]. Initially developed for the simulation of complex optical devices ("sequential raytracing" mode), OpticStudio indeed offers a simulation mode dedicated to OWC-type applications ("non-sequential raytracing" mode), in which the rays can interact with obstacles in the environment in any order. However, the computation time remains very high, and the GBDM methods are intrinsically limited to a given scenario, so they cannot be easily transposed to other environments without a precise modelling of the latter.

2.2.2   Stochastic Methods

Stochastic methods are the second major category of OWC channel modelling techniques. These are based on modelling, according to certain probability distributions, elements of the geometry of the OWC link (e.g., the distribution of reflectors), and/or of the optical transmitters/receivers (e.g., the number and direction of transmitted or received light rays). According to Al-Kinani *et al.* these methods can be categorized as geometry-based stochastic methods (GBSM) or non-GBSM. In the first case, the interaction between the transmitted

signal and the environment is modelled by describing geometrical relationships between the effective reflectors, that may be generated randomly. The impulse response and the gain of the OWC channel may thus be modelled according to simple analytical formulas that can be based on known probability distributions [JNH02, HI07, CC05]. These methods are therefore very simple to use, but contain potentially large estimation biases, especially with respect to the influence of diffuse components. Advanced GBSM have however lately been proposed, like regular-shape GBSM (RS-GBSM) [AWH16] and 3D semi-GBSM [ZWH22], which can cope with space-time non stationarity of the OWC channel, special LED radiation patterns, motion speeds and arbitrary rotation and orientation of the sensors.

The non-GBSM methods are mainly based on the RT associated with the Monte-Carlo stochastic integration technique. They consist in launching rays in random directions from one of the sensors, then materializing each propagation path by a succession of reflections on the surfaces encountered, in randomly chosen directions. The optical power carried by each contribution is then calculated using the bidirectional reflectance distribution function (BRDF) of the encountered surfaces as well as the geometric characteristics of the ray (e.g., angle, length). These methods have, compared to radiosity methods, the advantage of being applicable to any type of reflective surface, and not only to Lambertian reflectors. Moreover, their computational complexity varies linearly with the depth of reflection considered, so that their degree of accuracy depends directly on the number of rays launched and is generally characterized by the variance of its estimator.

The use of this type of method was proposed for the first time by López-Hernández *et al.* in 1998, under the name of Monte-Carlo algorithm (MCA), which allowed to take into account perfectly diffuse and specular reflecting materials [LPS98a]. Although faster than the deterministic methods proposed at the time, this MCA approach nevertheless requires the launching of a much larger number of rays than those which will be effectively detected by the receivers, a large part of them being lost after multiple reflections. In [LPS98b; PJ00], the same research group therefore proposed a Modified Monte Carlo algorithm (MMCA), which ensures that each launched ray will contribute to the impulse response, thus reducing the variance of the Monte Carlo estimator.

Subsequently, the Blinn-Phong BRDF was first introduced in an optical channel simulation [RPL02], as well as the dependence of BRDFs on emitted wavelengths [RPR13]. Coupled with an accelerating structure for computing the intersection of the rays with the propagation environment and techniques for parallelizing the simulation algorithm, these methods allow the simulation of the impulse responses of OWC channels in complex environments with formats derived from CAD tools. It may be noted that to some extent, the "non-sequential raytracing" mode of OpticsStudio is similar to these optimized MMCA methods, but presents nevertheless lower performance.

A variant of the Monte-Carlo methods, called photon tracing algorithm (PTA), has been proposed in parallel by Lee in [LEE09]. Faster than the MMCA method, it is nevertheless less accurate. More recently, the Combined Deterministic and Modified Monte-Carlo (CDMMC) method has been proposed by Chowdhury *et al*. [CZK14]. It consists in calculating the first order contribution to the impulse response using a radiosity method, then using the stochastic MMCA method from each reflector for the higher order contributions, which allows to reduce the computation time for second order reflections and below but induces nevertheless computation times more important than the MMCA method for higher reflection depths.

Purely Monte-Carlo methods thus seem to be remained among the most relevant for fast channel impulse response simulation in complex environment, which is why they are at the basis of the works carried out by Behlouli *et al*. In [BCA17], this team presents a Markov-chain Monte Carlo (MCMC) method, which reduces the number of light rays that must be simulated to achieve a given accuracy threshold by automatically focusing on the paths that transport more power. The MCMC method thus reduces dramatically the computation time necessary to reach a given quality compared to the MMCA method or OpticsStudio. In [CJJ20], it is used to investigate the impact on the OWC channel of the characteristics of the environment model, such as the level of geometric description, the reflectivity of materials, but also the influence of the ambient noise induced by the sun and of the user mobility, in the specific case of an aircraft cockpit.

3   Scenario and Applications

The 6GBRAINS channel model covers the following scenarios:

- Large industry hall
- Machine room
- Laboratory

The following applications have been tested and considered during the development of the channel model:

- Fixed point-to-point link for back and front hauling applications
- Access point to mUE

The example in Figure 5 shows the industry hall scenario (Bosch plant in Blaichach) with three different APs: AP1 with sub-6 GHz radio interface for mobile users and 200 GHz for front-hauling, AP2 with co-located sub-6 GHz and mmWave for mobility, and sub-THz radio interface for front-hauling, and AP3 with distributed OWC interfaces for mobility and sub-THz for front-hauling. This scenario covers most of the different applications described previously.
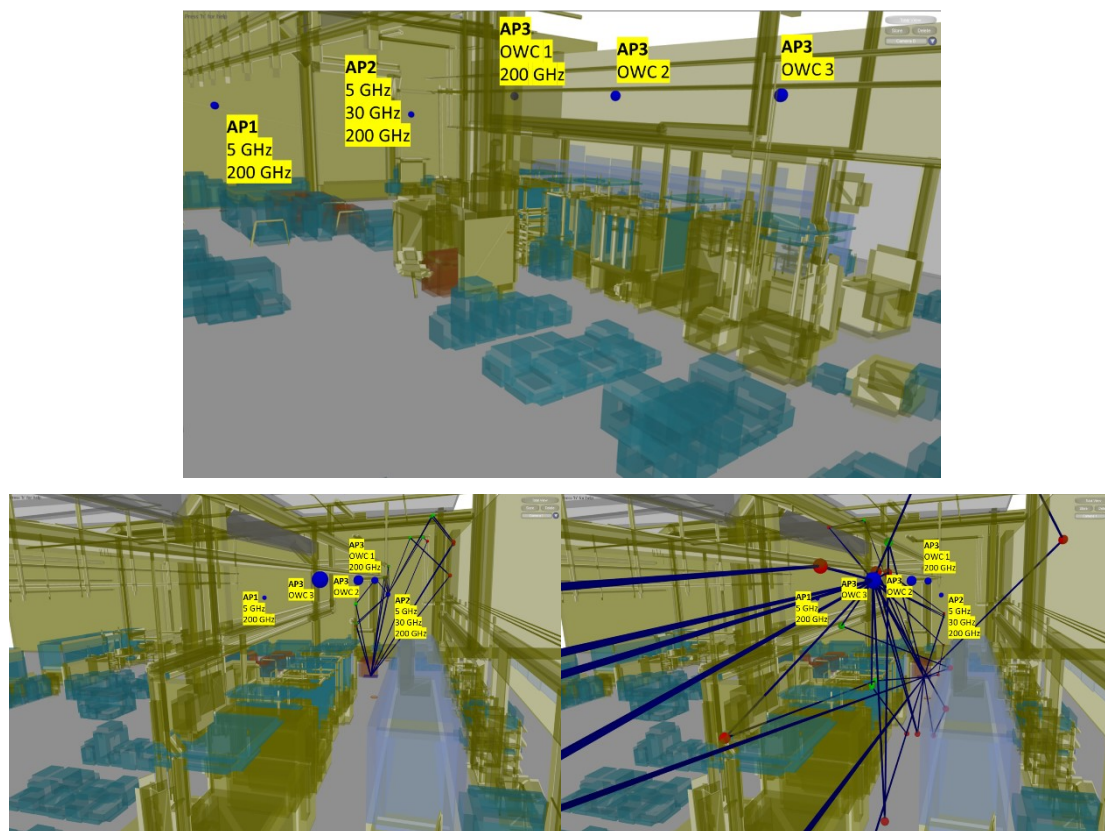
Figure 5: RT simulation results of the isotropic multi-path components for a single mUE position connected to AP2 at 30 GHz and AP3 in OWC 3 interface (20 rays simulated).

3.1   Machine Room Scenario

The machine room scenario is in the facilities of Fraunhofer in Ilmenau, Germany. The dimensions of the room are 6.48 m × 10.05 m × 6.33 m and there are different tools typically

found in industrial and machine halls, as shown in the 360° pictures taken from one of the TX and one of the RX positions in Figure 6, respectively. The predominant constructive materials of the different items are iron, steel, aluminium, plexiglass, concrete, and steel sheet. This scenario can be easily compared to a portion of a production line. The main component in the room is a computer numerically controlled (CNC) milling machine located in the centre of the room.

(a)

(b)

Figure 6: Picture of the machine room scenario.

The workflow to obtain the map of the RT model from point-cloud is similar to what was presented in D3.1, and it is repeated in Figure 7.

Figure 7: Workflow for point-cloud to RT model.

Scanning of the environment.

The Leica BLK360 laser scanner was used in this room. It is useful to have more than one recording position as some areas of the environment would not be recorded due to blockage of some objects. In this case, as shown in Figure 8(a), the scanner was set in four different recording positions to avoid blind spots in the environment.

Connect and merge the point-cloud.

After all recordings have been made, they must be merged, and a final point-cloud must be registered. Leica Cyclone REGISTER is the most popular software for registering laser scan data and it has also been used in this case. Figure 8(b) shows the final point cloud by their color and by the points intensity.

Modelling.

Modelling process is the most time-consuming process in the workflow. It requires a lot of manual work. In this process, every object in the environment is reconstructed by primitive blocks – such as boxes or cylinders – with the help of the point cloud. Although some objects, e.g., pipes or commonly used metal profiles, can be reconstructed easily while using best fit modelling tools, in most of the cases, the shape, position, and size of a block has to be adjusted manually. The Cloudworx AutoCAD Pro Add-On allows the user to interact with every single point or certain areas of the point-cloud and therefore accelerates the modeling process. Figure 8(c) shows the resulting AutoCAD model of this industrial alike environment. The model consists of a total of five layers – one for each material. They can be distinguished by their colors.

Triangulation and material assignment

Once the model is ready, it can be exported using stereolithography (.stl) format since it can be read from raytracing simulations software. Afterwards, the model can be imported, and material properties can be assigned directly in the simulation software, as shown in Figure 8(d). In the present model, we have considered the materials metal, plastic, concrete, wood, and glass.

(a)   (b)   (c)   (d)
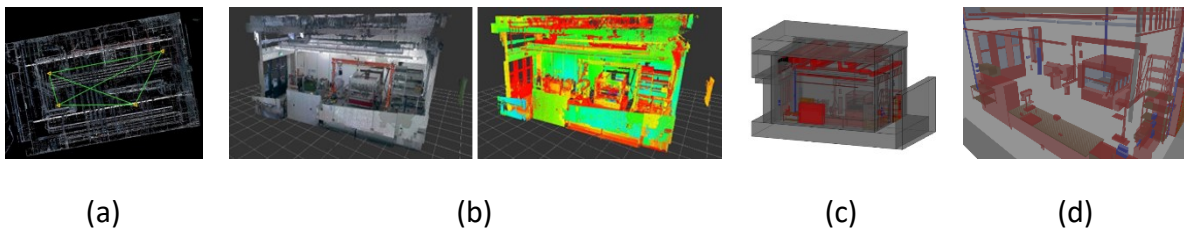
Figure 8: Different stages of the workflow from scanning to RT model for the machine room scenario.

3.2   Laboratory Scenario

The electronics laboratory scenario is in the Institut supérieur d'électronique de Paris (ISEP). The dimensions of the room are 9.58 m × 3.44 m × 2.5 m and there are different instruments and furniture typically found in electronics laboratory, as shown in the 360° panoramic pictures in Figure 9. The main component in the room is an electronic experimental bench and there is an exchange discussion area located in the centre of the room.

(a)
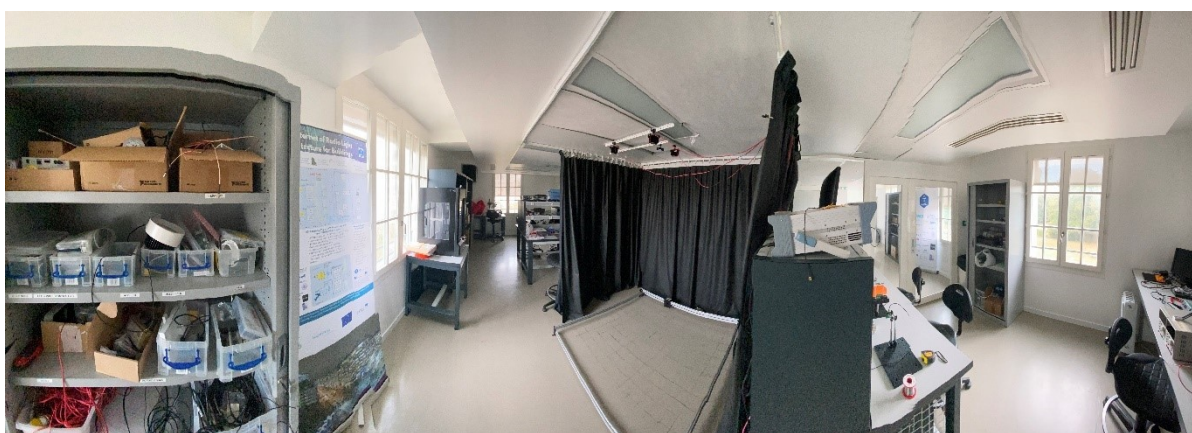
(b)

Figure 9: Picture of the electronics laboratory scenario.

Scenario Modelling

The scenario was modelled using the Polycam software installed in iPad was exploited to scan the 3D model of the scenario. Figure 10 shows the 3D model of the electronics laboratory scenario.
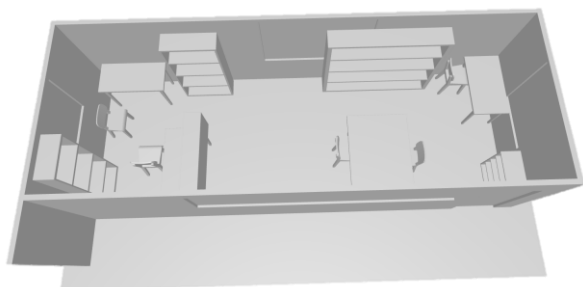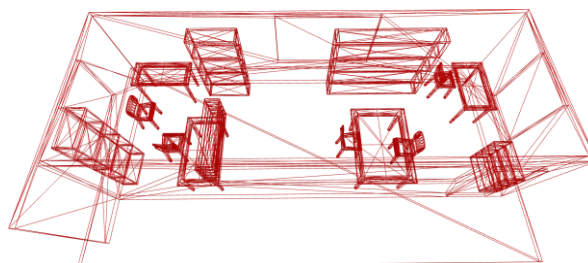
(a)   (b)

Figure 10: 3D model of the electronics laboratory scenario.

4   Hybrid Deterministic/Stochastic Multi-band RF Physical Model based on Raytracing.

The objective of this model is to provide a realistic deterministic baseline in the simulation results, which is enriched with stochastic components that can neither be generated by the discrete nature of the maps for RT simulations, nor the computation properties of the underlying simulation tools based on raytracing.

Moreover, most of the available commercial (e.g., WinProp) and non-commercial (e.g., Sionna, MATLAB) tools allow simulations up to 100 GHz. Therefore, a certain amount of post-processing must be done on the simulation results to adequate the data to the target simulations. One of the main limitations is the parametrization of the electromagnetic properties of the different constructive materials. Hence, in 6G BRAINS we have used latest measurement results found in the literature to interpolate reflection losses and compensate them in post-processing steps considering the frequencies of interest. In addition, free-space propagation loss of each path and Doppler shifts must also be compensated. On the other hand, aspects as diffraction require the re-computation of coefficients in which the geometrical properties of the interacting objects are needed. The output of the RT simulations usually doesn't provide this information and therefore can't be compensated. However, as seen in the Deliverable D3.3, diffraction is very low and therefore these paths can be in the worst case neglected. This modelling methodology approach is summarized in Figure 11.

(a)

(b)
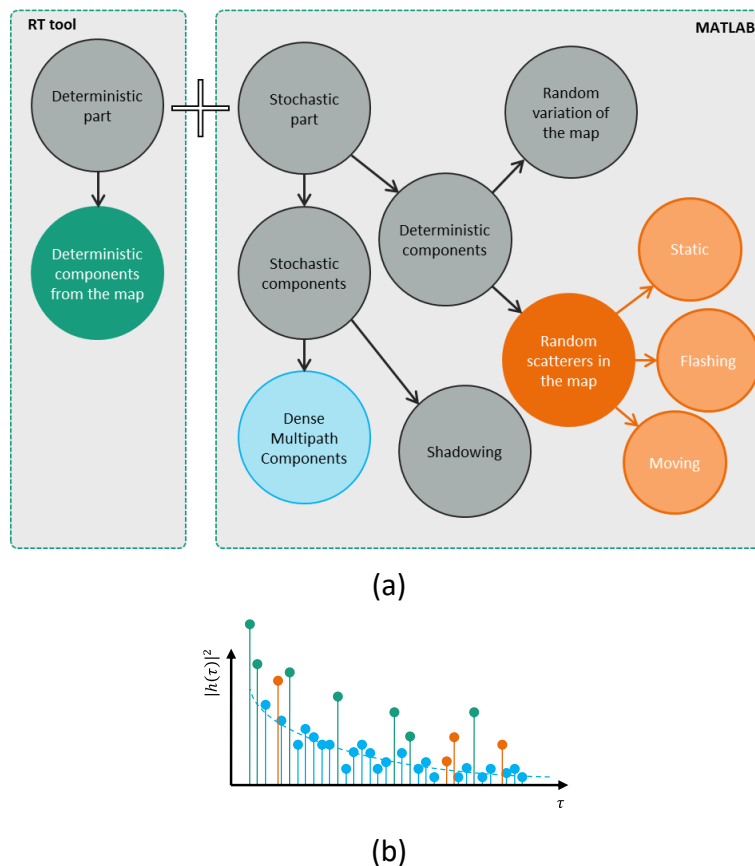
Figure 11: (a) 6G BRAINS stochastic/deterministic model structure and (b) example of CIR with the different deterministic and stochastic components.

4.1   Channel Impulse Response

The equivalent baseband multi-dimensional channel impulse response in the frequency band f_c at the jth TX and i^{th} RX antenna consists of a deterministic and a stochastic part:

$$h_{i,j}(t,\tau,f_c) = h_{i,j}^{\text{det}}(t,\tau,f_c) + h_{i,j}^{\text{sto}}(t,\tau,f_c).$$

The classification between deterministic and stochastic is in this case from the scenario point of view. The deterministic part consists of the MPCs corresponding to the map of the scenario under test. On the other hand, within the stochastic part, we still can have deterministic components, e.g., randomly created clusters but whose geometrical properties are still deterministically calculated.

Differently, purely stochastic components in the channel refer to MPCs or events that are not calculated or generated deterministically, e.g., unresolvable DMCs. They are randomly generated from distributions parametrized from measurements. These components represent all the energy in the environment, product of weak diffracted or diffuse scattered paths that the system cannot resolve. Moreover, events as shadowing of paths are also determined purely stochastically.

Therefore, as shown in Figure 11, the physical modelling approach followed in 6G BRAINS considers a deterministic underlaying base model from RT simulations in realistic maps obtained from precise LiDAR scans of the environments under investigation, with a set of stochastic components calculated in a post-processing phase, implemented in MATLAB. However, this stochastic part contains both deterministic and stochastic paths and events (as shadowing). The workflow with WinProp and MATLAB related to the different deterministic/stochastic components are summarized in Figure 12.
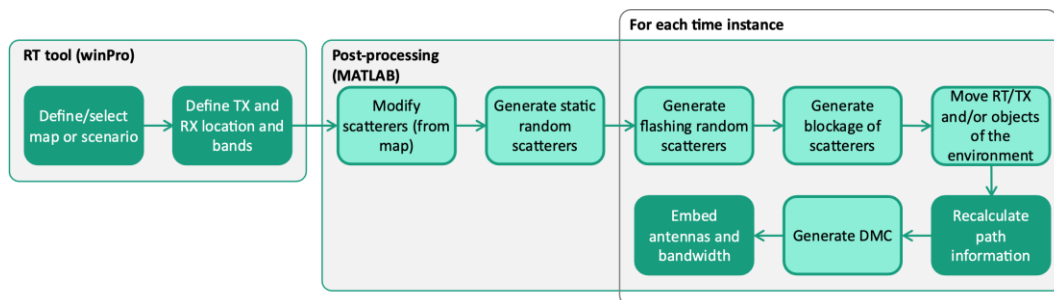
Figure 12: Workflow of the deterministic/stochastic model.

Within 6G BRAINS, we have validated the creation and parametrization from measurements of the following components, shown in Figure 13:

- Deterministic part
  - Deterministic map of the environments of interest
- Stochastic part
  - Dense multipath components
  - Random variation of the map

     o   Random scatterers in the map: static
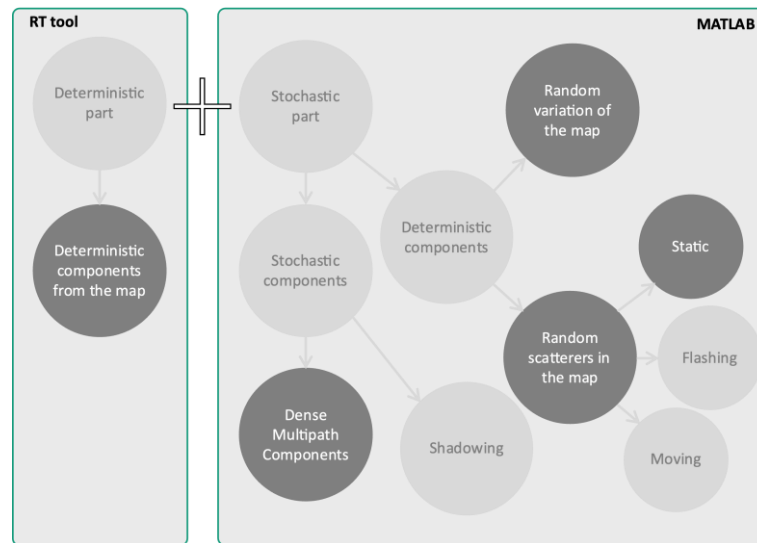
Figure 13: Deterministic and stochastic components addressed from measurements in this Deliverable.

4.2 Deterministic Components

There are two sources of deterministic components in the model: the deterministic paths calculated by the RT tool, and the deterministic paths randomly generated in the post-processing step.

The deterministic components from the deterministic part are calculated from standard RT, in this implementation, using the Altair WinProp© software. Different precise maps with multiple details have been derived from 3D LIDAR scans (see D3.1) and parametrized with the electromagnetic properties of the different constructive materials.

The output of the RT simulation for each frequency band f_c and position in the map is a set of L rays with the following parameters:

- τ_l: time of flight (delay),
- ϕ_{A_l}: azimuth of arrival,
- θ_{A_l}: elevation of arrival,
- ϕ_{D_l}: azimuth of departure,
- θ_{D_l}: elevation of departure,
- $\gamma_l^{\phi\phi}$: amplitude in the TX ϕ – RX ϕ polarization,
- $\gamma_l^{\phi\theta}$: amplitude in the TX ϕ – RX θ polarization,
- $\gamma_l^{\theta\phi}$: amplitude in the TX θ – RX ϕ polarization,
- $\gamma_l^{\theta\theta}$: amplitude in the TX θ – RX θ polarization,

Each lth path is subdivided in different segments every time there is an interaction with an interface, providing the following information:

- *Object Id* and *Material Id*
- 3D coordinates of the interaction point of the object $\mathbf{p}_o$
- Type of interaction point (reflection, transmission, scattering).

The multi-dimensional dual-polarized SISO CIR $\mathbf{H}(f_D, \tau, \phi_A, \theta_A, \phi_D, \theta_D)$ can be constructed with these parameters and represented as a matrix:

$$\mathbf{H}^{\text{det}}(f_D, \tau, \phi_A, \theta_A, \phi_D, \theta_D, f_B) = \cdots$$

$$\cdots \sum_{l=1}^{L} \underbrace{\begin{bmatrix} \gamma_l^{\phi\phi} & \gamma_l^{\theta\phi} \\ \gamma_l^{\phi\theta} & \gamma_l^{\theta\theta} \end{bmatrix}}_{\boldsymbol{\Gamma}_l} \delta(\tau - \tau_l)\delta(f_D - f_{D,l})\delta(\phi_A - \phi_{A_l})\delta(\theta_A - \theta_{A_l})\delta(\phi_D - \phi_{D_l})\delta(\theta_D - \theta_{D_l}),$$

where L is the number of MPCs, and $\boldsymbol{\Gamma}_l \in \mathbb{C}^{2\times 2}$ is the dual-polarized complex scattering matrix considering the reflection/scattering/penetration and path-loss of each path, and $f_{D,l} = \frac{f_c}{c_0}\mathbf{r}_{RX,l}^T \boldsymbol{v}$ is the Doppler shift of the lth path, where $\mathbf{r}_{RX,l}^T$ is the spherical unit vector at the RX,

$$\mathbf{r}_{\text{RX},l}^T = [\cos\theta_{A,l}\cos\phi_{A,l} \quad \cos\theta_{A,l}\sin\phi_{A,l} \quad \sin\theta_{A,l}],$$

And $\mathbf{v}$ is the RX velocity vector consisting of the unit spherical vector times the scalar speed of the RX,

$$\mathbf{v}^T = v_{\text{RX}} \cdot [\cos\theta_{\text{RX}}\cos\phi_{\text{RX}} \quad \cos\theta_{\text{RX}}\sin\phi_{\text{RX}} \quad \sin\theta_{\text{RX}}].$$

The discrete time-varying CIR is calculated in the *fromRTtoCIR* function considering the system properties:

- antennas,
- bandwidth.

The MPCs obtained with the RT are integrated with the system properties into the time-varying frequency response of the channel. The band limited frequency response of the ith antenna at the RX and j^{th} antenna at the TX is calculated as

$$H_{i,j}^{\text{det}}(t_k, f_n, f_c) = \cdots$$

$$\cdots \sum_{l=1}^{L} \begin{bmatrix} G_{\phi,i}^{\text{RX}}(\phi_{A,l}, \theta_{A,l}) \\ G_{\theta,i}^{\text{RX}}(\phi_{A,l}, \theta_{A,l}) \end{bmatrix}^T \begin{bmatrix} \gamma_l^{\phi\phi} & \gamma_l^{\theta\phi} \\ \gamma_l^{\phi\theta} & \gamma_l^{\theta\theta} \end{bmatrix} \begin{bmatrix} G_{\phi,j}^{\text{TX}}(\phi_{D,l}, \theta_{D,l}) \\ G_{\theta,j}^{\text{TX}}(\phi_{D,l}, \theta_{D,l}) \end{bmatrix} \cdot \underbrace{\exp(-j2\pi f_n \tau_l)}_{\text{Frequency/delay duality}} \cdots$$

$$\cdots \underbrace{\exp\left(\frac{j2\pi f_c}{c_0} t_k \, \mathbf{r}_{\text{RX},l}^T \mathbf{v}\right)}_{\text{Time/Doppler duality}} \underbrace{\exp\left(\frac{j2\pi f_c}{c_0} \mathbf{r}_{\text{RX},l}^T \mathbf{p}_i\right)}_{\text{Steering vector at RX}} \underbrace{\exp\left(\frac{j2\pi f_c}{c_0} \mathbf{r}_{\text{TX},l}^T \mathbf{p}_j\right)}_{\text{Steering vector at TX}},$$

where $\mathbf{r}_{\text{TX},l}^T$ is the spherical unit vector at the TX,

$$\mathbf{r}_{\text{TX},l}^{T} = [\cos\theta_{D,l}\cos\phi_{D,l} \quad \cos\theta_{D,l}\sin\phi_{D,l} \quad \sin\theta_{D,l}].$$

and $\mathbf{p}_i$ and $\mathbf{p}_j$ are the local spherical coordinates of the ith antenna at the RX and j^{th} antenna at the TX, respectively.

The sampling points in the frequency domain are determined by the bandwidth of the signal and number of samples:

$$f_n = \Delta_f n,$$

where $\Delta_f = \frac{B}{K_f}$ is the sub-carrier spacing, B is the total bandwidth, and K_f are the total amount of sub-carriers. Similarly, in the time domain,

$$t_k = \frac{T}{K_t}k,$$

where T is the total time interval, and K_t is the amount of time samples.

4.2.1 Deterministic Displacement of RX

Depending on the number of rays, interactions, and size of the scenario, the re-calculation of all the MPCs for each new position of a moving RX can result in practically impossible computational times for RT.

Therefore, in this implementation of the model, under several assumptions, we simulate with the RT software different positions in the scenario with a large grid in terms of wavelength (from the sub-THz point of view). Then, the channel model synthesizer (*reTrace* function) implemented in MATLAB re-traces all the MPCs for the new position of the RX for the different time instances. This allows in a cost-efficient way, to obtain sampling points of the channel at different speeds of the mobile terminal and at sampling times that allow Doppler resolution. However, this is possible only under the assumption that the interaction points of the MPCs act as point-scatterers: the reflection losses don't change with the different impinging and reflected angles.

The RT provides for each ray the coordinates of the different interaction points $\mathbf{p}_o$. Therefore, the recalculation of the geometrical properties (DoD, DoA, and delay) of each segment within the path is straightforward. This is implemented in the recursive *reTrace* function that accepts as input the current RT CIR with the updated positions of the RX and the interaction points, the time instance, and the velocity vector to update the RX position.

The updated coordinates of the RX $\mathbf{p}_{\text{RX}}^{T}$ in the time instant t_k is calculated by

$$\mathbf{p}_{\text{RX}}^{T}(t_k) = \mathbf{p}_{\text{RX}}^{T}(t_{k-1}) + \Delta t \, v_{\text{RX}} \cdot [\cos\theta_{\text{RX}}\cos\phi_{\text{RX}} \quad \cos\theta_{\text{RX}}\sin\phi_{\text{RX}} \quad \sin\theta_{\text{RX}}].$$

With the updated RX coordinates, the calculation of the DoD, impinging and reflected angles in the intermediate interactions, the DoA and delays are easily re calculated. Of special importance is the DoA to estimate the phase difference over time of each MPC to account for Doppler. Afterwards, within the *reTrace* function, the different geometrical properties and path-gain (considering only the extra losses given by the larger propagation distance by free-space) of all the sub-paths are re-calculated using the new position of this object.

The verification of the performance of this method has been done by comparing the Doppler spectra of a RX using the *reTrace* function and the "empirical" Doppler spectra using a fine simulation grid smaller than half of the wavelength with the RT software (which is computationally expensive). The power delay profiles for both cases are shown in Figure 14. There is a slight difference on the RT + retracing result given by the point-scatterers assumption and the life span of path. While in "reality", the path seen in Figure 14a slightly earlier than 30 ns in delay is changing the gain accordingly to the position of the RX. However, this path has constant gain in Figure 14b due to the point-scatterer assumption. This produces a sharper peak at approximately 500 Hz in the Doppler spectrum in Figure 14c.

(a)   (b)

(c)
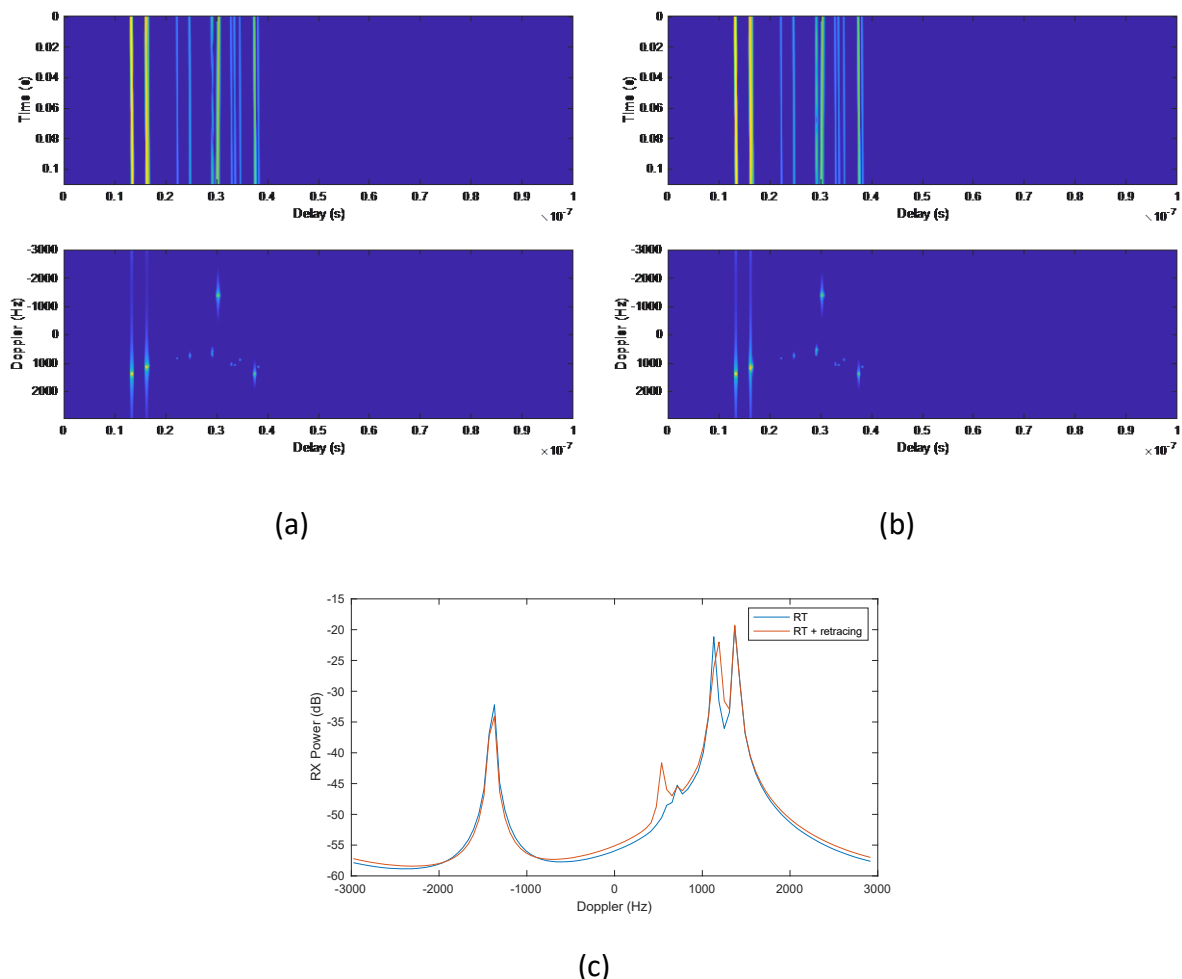
Figure 14: comparison of "empirical" Doppler power spectrum and the result of the reTrace function. Power delay profile and power delay/Doppler spectrum with (a) pure RT simulations and (b) retrace function. (c) Power Doppler spectrum for RT (empirical) and RT + reTracing.

4.2.2   Deterministic Displacement of Randomly Selected Objects in the Scenario

Different objects from the map can be selected and moved in a post-processing step during the simulation. The new location of the object, the delay, directions of arrival and departure, and difference on amplitude product of the new path-loss are re-calculated with the implemented function *reTrace*.

However, this approach considers the scattering objects as point-scatterers, and the scattering properties don't depend on the incident or reflected angles. Fresnel coefficients are also not re-calculated and there is only a change on the path gain due to the difference on path-loss. In addition, the new position of the objects neither generates new MPCs nor blocks previously calculated MPCs.

The RT simulator provides for every interaction of the rays with an object, a unique identification *Object_ID* and the vector of coordinates $\mathbf{p}_o$ of the interaction point. The *reTrace* function requires the moving object ID, and the velocity vector (scalar velocity v_o and the direction of displacement given by the unit vector in the azimuthal ϕ_o and elevation θ_o directions).

For every time instant t_k, the coordinates of the moving objects are re-calculated by applying the spatial translation,

$$\mathbf{p}_o^T(t_k) = \mathbf{p}_o^T(t_{k-1}) + \Delta t \, v_o \cdot [\cos \theta_o \cos \phi_o \quad \cos \theta_o \sin \phi_o \quad \sin \theta_o].$$

Afterwards, within the *reTrace* function, the different geometrical properties and path-gain of all the sub-paths are re-calculated using the new position of this object.

4.2.3   Random Variation of Deterministic Multipath-Components from the Map

This option adds random variations on the amplitude of the MPCs resulting from the different interaction types for every run of the simulations. Therefore, the resulting simulations represent the same scenario in a more generic manner, since for each run, the underlaying scenario is represented with a slight variation of the different scattering properties of the objects.

The implementation procedure is as follows. For every simulation run,

1. Random selection of the **number of objects** to be modified in the map,
    $$N_{obj} \sim \mathrm{unif}(0, N_{total}),$$
    where N_{total} is the total number of objects in the simulation.

2. Random selection of N_{obj} **objects**
    $$n = \left\{ o_{ID,1}, o_{ID,2}, \dots, o_{ID,N_{obj}} \right\},$$
    where o_{ID} is the unique index identifier of the different objects.

3. Deterministic or random ([PKJ13]) generation of the modifying factor of the properties of the material for each object in n,

    $$\alpha_n^{\mathrm{sto}}(f_c) \in \mathbb{C}.$$

Measurements from 2 to 170 GHz have shown that there is a clear relation on frequency and the penetration loss [ACC22a], but not in the reflection loss for most of the materials under test, [ACC22b]. Similar results have been discussed in ITU-R P.2040-2 [ITU19] and METIS [MET15]. Hence, if the interaction type is a transmission, the extra coefficient is scaled with a frequency band dependent value. On the other hand, if the interaction type is a reflection, there is no scaling with frequency in most of the cases. A simplified linear relation between the frequency band f_c and the transmitted power (penetration loss) and reflected power (reflection loss) is obtained from the plots presented in [ACC22a] and [ACC22b] for many different materials:

$$\alpha_n^{\text{sto}}(f_c) = 10^{\frac{a - b \cdot f_c}{20}} \cdot \exp(j\phi_n)$$

where $\phi_n \sim \text{uniform}(-\pi, \pi)$. The model parameter a and b can be set deterministically from Table 1 or stochastically generated from uniform distributions limited by the extreme cases from the same table.

In addition, if the roughness of the surface is proportional to the carrier frequency, the reflection includes extra losses due to the diffuse scattering calculated as

$$\rho_s = \exp\left(-8 \left(\frac{\pi \sigma_h \cos(\phi_i) f_c}{c_0}\right)^2\right),$$

where σ_h is the standard deviation of the zero-mean height of the surface and ϕ_i is the incident angle [LFR96]. The resulting reflection coefficient is then calculated as

$$\alpha_n^{\text{sto}}(f_c) = \alpha_n^{\text{sto}}(f_c)\rho_s$$

Table 1: Parameters of the model for the frequency dependent penetration and reflection loss for different materials.

Material	Width	Transmission	Reflection	Orientation
Aerated concrete	70 mm	-	$a = -13$ $b = 0$	H/V
Laminated glass	8 mm	$a = -1$ $b = 0.0813$	$a = -13$ $b = 0$	H
Blurred glass	3 mm	$a = -1$ $b = 0.0563$	$a = -5$ $b = 0.0625$	H
Plexiglass	19 mm	$a = -0.5$ $b = 0.0187$	$a = -15$ $b = 0$	H
Composite fiber panel	14 mm	$a = -0.5$ $b = 0.0375$	$a = -22$ $b = 0$	H/V

Plywood	22 mm	$a = -1$ $b = 0.1625$	$a = -15$ $b = 0$	V
Laminated wood	22 mm	$a = -1$ $b = 0.25$	-	V
Medium density fiber (MDF)	22 mm	$a = -1$ $b = 0.1187$	$a = -13$ $b = 0$	H/V
Plasterboard BA13	13 mm	-	$a = -15$ $b = 0$	H/V
Plasterboard BA18	18 mm	-	$a = -13$ $b = 0$	H/V
Mortar (Cement plus sand)	22 mm	-	$a = -20$ $b = 0$	H/V
Glass wool	19 mm	-	$a = -10$ $b = 0$	H/V
Polystyrene	19 mm	-	$a = -38$ $b = 0$	V
Floor vinyl tile	4 mm	-	$a = -7$ $b = 0$	H
Floor ceramic tile	8 mm	-	$a = -5$ $b = 0$	H
Office carpet	4 mm	-	$a = -3$ $b = 0$	H

The modelled penetration and reflection loss of the materials are presented in Figure 15.
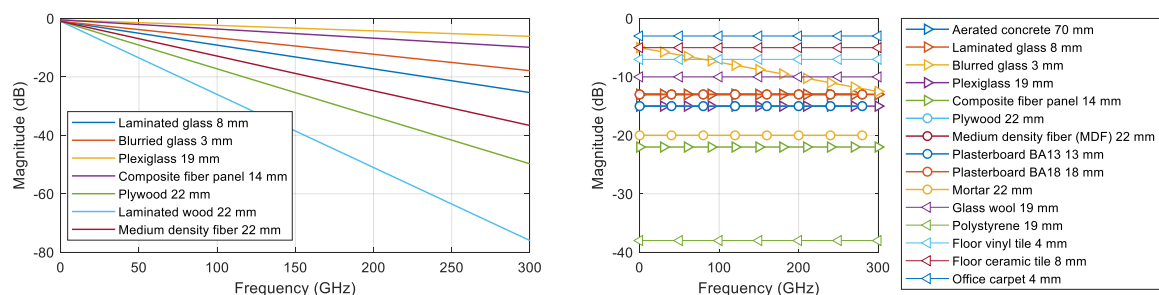
Figure 15: Penetration and reflection loss for different materials.

4. The amplitude of every MPC calculated with the RT in the underlaying model that is interacting with object O_n is multiplied by Γ_n.

This modelling methodology accounts for a random incident/reflected angle independent variation of amplitude and phase for different frequencies.

However, it is worth mentioning that this variation depends on the frequency and incident and reflected angles. The methodology previously described still provides spatial consistency in terms of the incident angles, but not on the amplitude and polarization of the MPCs.

4.2.4   Random Paths

As well as in other hybrid deterministic/stochastic channel models [PK13, WPK16], random components are included to account for the contribution of missing scatterers and enrich the limited number of elements in the map. In addition, since they are recalculated with every run of the simulation, they also change the environment to generate a slightly different scenario on every run (stochastic environment). These components can be present during the complete run of the simulation (unless they are shadowed), or they can appear and disappear.

4.2.4.1   Static Paths

These paths are defined as point-like scatterers and are set to appear during the complete simulation time. The position in space of the scatterers is arbitrarily selected from random numbers within certain margins defined by the scenario size, as shown in Figure 16.

The number of interaction points of each path can be defined as a single order interaction point or higher order (undefined), in which case, only the position of the scatterers of the first and last interaction points is defined.

These scatterers are visible for all the frequencies, and the reflection/penetration/scattering properties can be randomly selected from a database (e.g., Table 1) or drawn from random distributions.

The implementation is as follows:

1. Define the number of random paths L_{sto}.
2. From the RT map, define a volume V in which the random scatterers will be located.
3. Randomly select L_{sto} points $\mathbf{p}_{\text{sto}}$ within the volume V.
4. Randomly assign reflection losses to each scatterer.
5. The function *reTrace* calculates the different delays, angles, and amplitude for each new path.

(a)   (b)
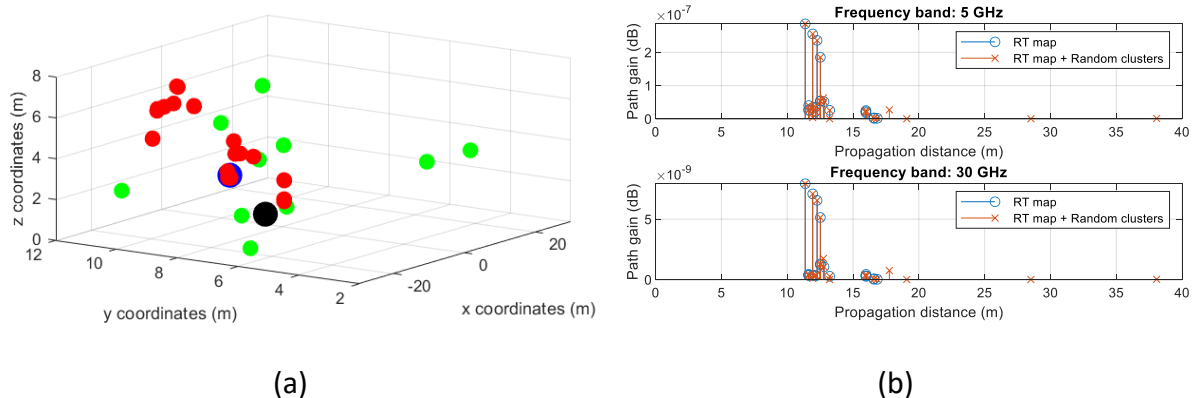
Figure 16: Example of RT map and random clusters (a) in space, and (b) the CIR.

The statistics of the DS calculated for each run generating up to $L_{\text{sto}} = 10$ random scatterers in a volume $V = 32 \times 12 \times 5$ m at 190 GHz is displayed in Figure 17, showing the influence of the random scatterers on the DS. The mean value of the generated DS considering the stochastic components with 1000 different runs is, in this example, 7.35 ns. This value is close

to 8.1 ns, the mean DS reported from measurements in this scenario in the Deliverable 3.3. Hence, the statistics generated from these components are within meaningful margins.
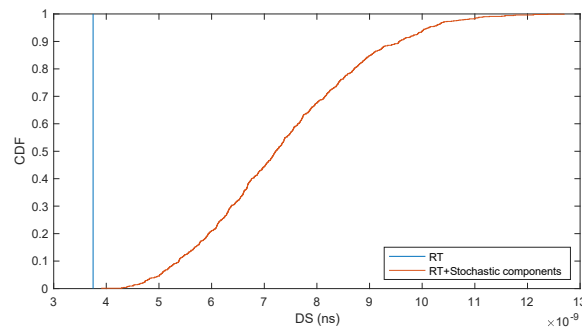
Figure 17: CDF of the DS with random scatterers in the environment.

There are several assumptions that limit the accuracy of this approach:

- Single bounce paths: the simulated scatterers correspond to first order reflections.
- Random selection of reflection losses: this can be further improved with a better parametrization. So far, the losses are randomly selected from the frequency dependent reflection losses from Table 1.
- Assumption of point-scatterers: the simulated scatterers act as point-scatterers with independent reflection losses to the incident angles.
- These scatterers are only related to a single AP – mUE link: two different mUE see different scatterers, even if they are closely located in the map. This can be improved by defining a correlation distance that governs the drop of these random scatterers in the map.

4.2.4.2 Flashing Paths

These clusters appear and disappear randomly over time and represent moving objects that generate a reflection over a short period of time.

4.2.4.3 Moving Paths

The moving paths are generated as randomly located objects in the environment with a deterministic displacement. The path parameters of a single bounce from TX to RX is deterministically calculated and included in the over CIR.

4.3 Stochastic Components

4.3.1 Dense Multipath Components

They represent multipath components that are not resolved by the system. The gain of the MPCs decreases exponentially with the propagation distance and the departure and arrival angles are uniformly distributed within certain margins. Measurements in [PSH11, DML20] have shown a certain correlation on the specular to DMC power ratio over the angle of departure and arrival. However, for sake of simplicity, spatial correlation of DMC is not

considered in this model. On the other hand, it is considered a frequency dependence on the decaying rate $\beta_{\text{DMC}}(f)$, as observed in measurements in industrial scenarios in [DML20],

$$P_{\text{DMC}}^{\text{pol}}(\tau) = \begin{cases} 0, & \text{if } \tau < \tau_{\text{DMC}} \\ \alpha_{\text{DMC}}(f) \cdot \exp\bigl(-\beta_{\text{DMC}}(f) \cdot (\tau - \tau_{\text{DMC}})\bigr), & \text{if } \tau \geq \tau_{\text{DMC}} \end{cases}$$

The model considers three different parameters: $\tau_{\text{DMC}} = \tau_{\text{3D}} + \Delta\tau$ is the starting delay of the DMC (where τ_{3D} is the delay of the LOS component, or in NLOS, the direct blocked path), α_{DMC} is the gain of the first DMC path, and β_{DMC} is the decaying rate.

This model can be linearized in the logarithmic scale (for $\tau \geq \tau_{\text{DMC}}$):

$$10 \cdot \log_{10}\left(P_{\text{DMC}}^{\text{pol}}(\tau)\right) = -10 \cdot \log_{10}(\beta_{\text{DMC}}(f)\,\tau) + 10 \cdot \log_{10}\bigl(\alpha_{\text{DMC}}(f)\bigr)$$

and the parameters estimated from linear regression of the power delay profile.

An approach utilizing room electromagnetics models the DMC as a process that depends on the size of the room and the frequency. In this approach, the PDP is divided in three regions: early components (EC, mostly local scattering with low order reflections) and reverberation,

$$P(\tau) = P_{EC}(\tau) + P_{DMC}(\tau).$$

The reverberation region may contain also strong late specular components. The starting time of the reverberation region has shown experimentally, to coincide with the mean delay, and is calculated as,

$$\tau_{DMC} = \frac{\int \tau P(\tau) d\tau}{\int P(\tau) d\tau}.$$

The other parameters are estimated per measured power delay profile pro band by linear regression of the reverberation region,

$$P_{DMC}(\tau) = -10 \cdot \log_{10}(\beta_{\text{DMC}}(f)\,\tau) + 10 \cdot \log_{10}\bigl(\alpha_{\text{DMC}}(f)\bigr).$$

Where the decaying rate is

$$\beta_{DMC} = \frac{10 \log_{10}(\alpha_{DMC})}{T_{rev}}.$$

The parameters for the different frequencies and visibilities are listed in Table 2.

Table 2: parameters for the DMC in industry hall scenario.

Visibility	Parameter/frequency		6.75 GHz	30 GHz	60 GHz
LOS	T_{rev} (ns)	Mean	130.6	147.1	113.9
		Std.	4.2	9.8	10.6
	α_{DMC} (dB)	Mean	-83.4	-104.2	-107.9
		Std.	0.8	3.0	2.0
NLOS	T_{rev} (ns)	Mean	141.1	134.3	109.0
		Std.	12.9	19	20.4
	α_{DMC} (dB)	Mean	-81.8	-104.9	-110.5
		Std.	1.3	1.7	2.2

An example of the reconstructed PDP in LOS in the measurements in the industry hall scenario by BOSCH in Blaichach is shown in Figure 18.
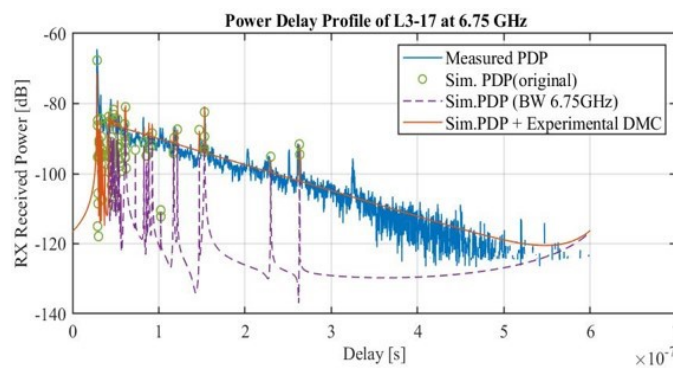
Figure 18: Reconstructed PDP with DMC components in industry hall scenario.

4.3.2 Shadowing of Components

Differently to the flashing components that appear and disappear randomly during the movement of the mUE, paths calculated deterministically from the map and random paths can be shadowed during the simulations. This phenomenon represents people or objects moving on the environment. While there are deterministic approaches on the shadowing of multipath components addressed in the 3GPP [3GP20], METIS [MET15], and MIWEBA [WPK16], in this model we follow a completely stochastic approach for sake of simplicity. Therefore, the attenuation of randomly selected MPCs within the CIR is calculated from a normal distribution parametrized from the empirical path-loss model for industrial scenarios.

5   Validation of the RT Model of the Machine Room Scenario from RF Measurements

5.1   Methodology

The deterministic components have been validated by comparing the measured and RT simulated marginal power profiles (delay, angular, and total received power). The same TX and RX positions are set in the RT tool as they were set during the measurements. For a fair comparison, the system aspects (bandwidth and antenna patterns) of the measurement equipment are embedded in the RT simulations, and the set-up is recreated as well (rotation of the directive antennas), as shown in the workflow in Figure 19.
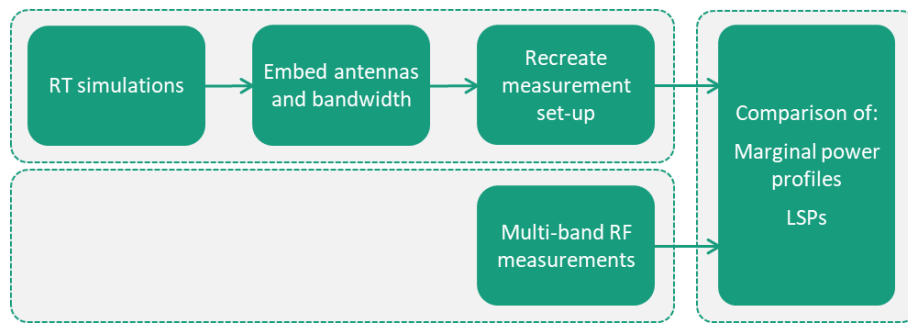
Figure 19: Workflow for validation of RT simulations with multi-band measurements.

The results of the RT simulations consist of a discrete representation of a limited number of multipath components. The CIR can be represented as a train of impulses as follows,

$$h_{RT}^p(\tau_l, \phi_l, \theta_l, \varphi_l, \vartheta_l) = \sum_l \alpha_l^p \, \delta(\tau - \tau_l)\delta(\phi - \phi_l)\delta(\theta - \theta_l)\delta(\varphi - \varphi_l)\delta(\vartheta - \vartheta_l), \quad (1)$$

Where, for sake of simplicity, $\alpha_l^p = \left\{\gamma_l^{\phi\phi}, \gamma_l^{\phi\theta}, \gamma_l^{\theta\phi}, \gamma_l^{\theta\theta}\right\}$ is the path amplitude for one of the possible TX-RX combinations of polarization. The antenna patterns at TX and RX, the process of rotating the antennas for the directional scans, and the measurement bandwidth can be embedded as follows:

$$H_{RT+Ant+BW}^p(k\Delta f, i\Delta\phi, j\Delta\theta, m\Delta\varphi, n\Delta\vartheta) = \cdots$$

$$\cdots \sum_k \sum_l \alpha_l^p \, G_{Rx}^p(\phi_l - i\Delta\phi, \theta_l - j\Delta\theta)G_{Tx}^p(\varphi_l - m\Delta\varphi, \vartheta_l - n\Delta\vartheta)e^{-j2\pi \, k\Delta f \, \tau_l}, \quad (1)$$

where $G_{Rx}^p(\phi, \theta)$ is the RX antenna pattern in the p polarization, $G_{Tx}^p(\varphi, \vartheta)$ is the TX antenna pattern in the p polarization and $i\Delta\phi, j\Delta\theta, m\Delta\varphi$, and $n\Delta\vartheta$ are the scanning directions in the RX azimuth and elevation, and TX azimuth and elevation, respectively. These values are set during the experiments and can be found in the Deliverable D3.3.

Finally, the CIR is calculated with inverse Fourier transform:

$$h^p_{RT+Ant+BW}(\Delta\tau, i\Delta\phi, j\Delta\theta, m\Delta\varphi, n\Delta\vartheta) = IFFT\left(H^p_{RT+Ant+BW}(\Delta f, i\Delta\phi, j\Delta\theta, m\Delta\varphi, n\Delta\vartheta)\right)$$

The synthetic omni-directional PDP for the p polarization is calculated summing the PDPs from all the angular scans at the TX and RX

$$P^p_{RT+Ant+BW}(\Delta\tau) = \sum_{\forall i, \forall j, \forall m, \forall n} \left|h^p_{RT+Ant+BW}(\Delta\tau, i\Delta\phi, j\Delta\theta, m\Delta\varphi, n\Delta\vartheta)\right|^2$$

The differences on the PDP from considering a pure train of impulses and the different system aspects is displayed in Figure 20. In this case, we emulate the measurement set-up in Deliverable D3.3, where the TX1 and RX1 are located at the same height, and 15° HPBW antennas are used at both sides of the link to scan in azimuth (0° elevation plane). The isotropical characteristic of the simulations make that several path from reflections in the ceiling and floor appear with a large gain in Figure 20(a). This is attenuated after considering the antenna pattern due to the high directivity (15° HPBW) in Figure 20(b). The effect of considering a finite bandwidth is displayed in Figure 20(c), and finally, the reconstructed synthetic omni-directional PDP (summing the PDP of different scans in angle at TX and RX) is shown in Figure 20(d).

(a)

(b)

(c)

(d)
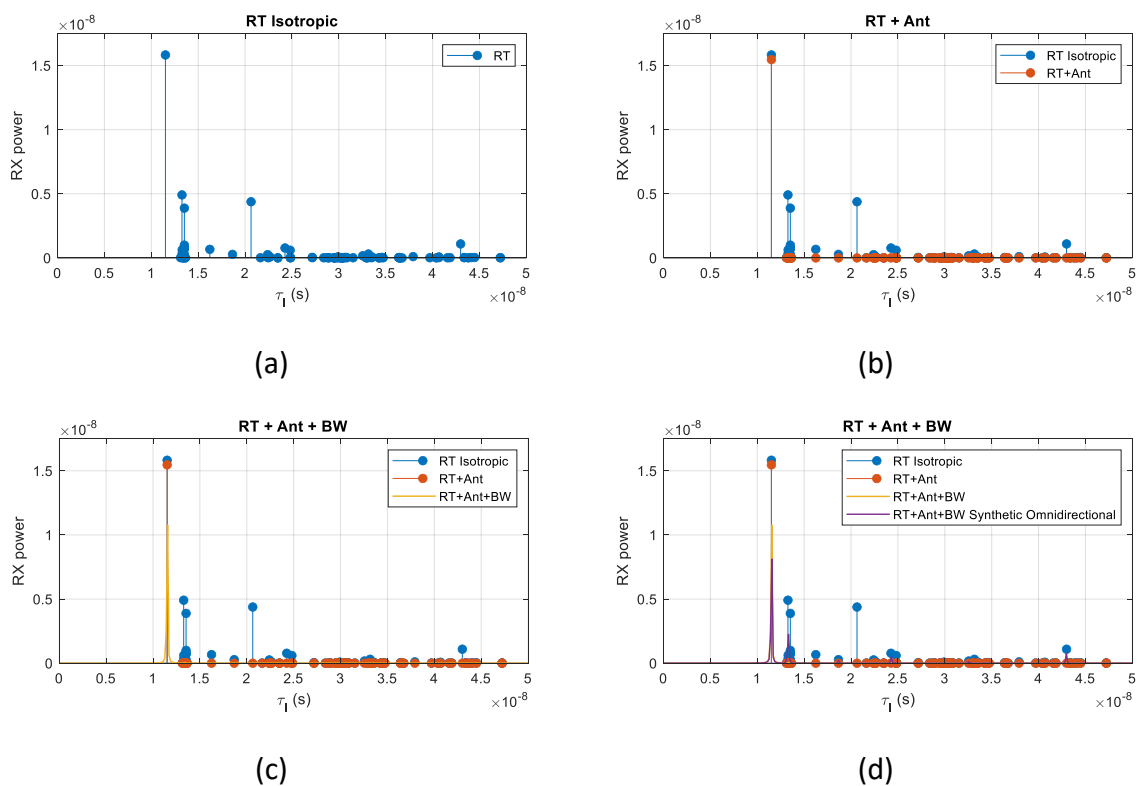
Figure 20: Effects of including system aspects into the RT simulations to compare with real-field measurements.

Similarly, the power azimuth/azimuth profiles considering pure RT simulations and after embedding the system aspects are displayed in Figure 21, where the effects of the antenna resolution can be observed. In addition, since only azimuth scans were performed, several strong multipath components that appear on the pure RT simulations (from ceiling and floor) in Figure 21(a) are later attenuated and almost no visible when considering antenna and bandwidth in Figure 21(b).

(a)   (b)
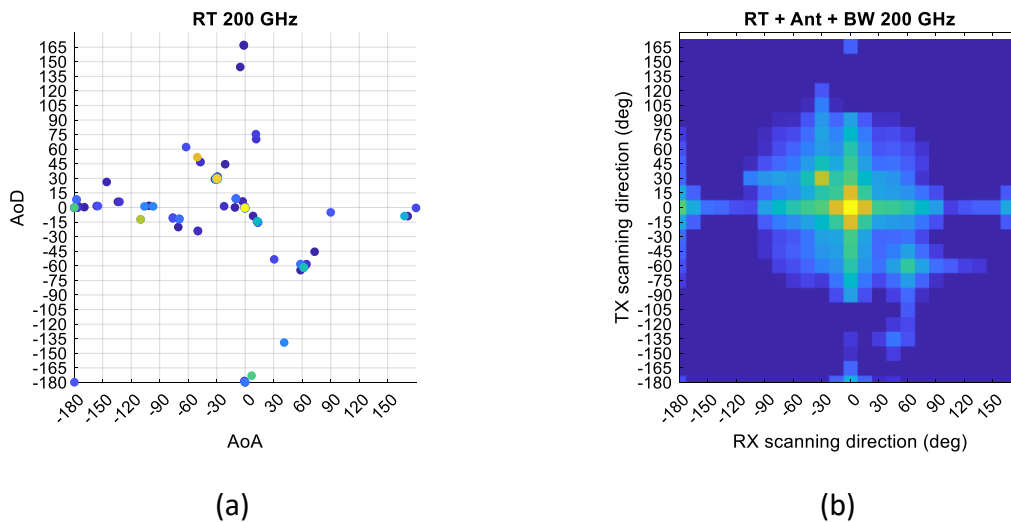
Figure 21: PAAP with (a) plain RT results, (b) considering system aspects as bandwdith, directivity of the antennas, and the rotation for scanning.

5.2   Map Validation from RT Simulations and Visual Inspection

The overlaying of the picture taken from the TX and RX during the RF measurements and the pure RT simulations in the same TX and RX positions are displayed in Figure 22 for the LOS measurement and in Figure 23 for the NLOS. In addition, some paths already analysed in the measurements in Deliverable D3.3 are marked and are used as references.

A very good match between the objects in the environment and the simulated rays can be observed. Examples are marked in yellow circles: pipes and light holders in the ceiling, the big crane, frames of the milling machine located on the right side in Figure 22(a), and also the small machine on the table at -45° azimuth and -15° elevation of departure.
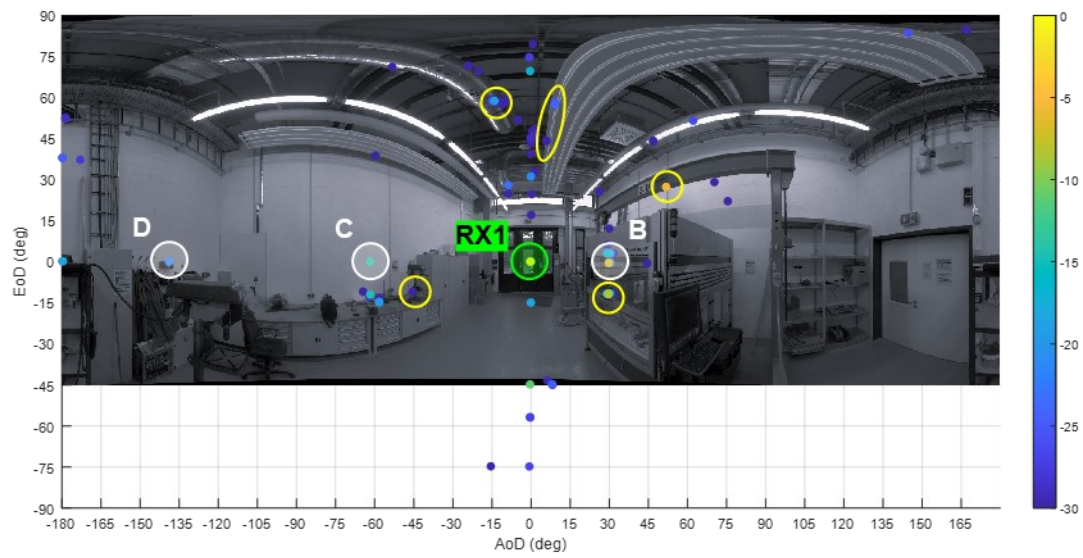
(a)
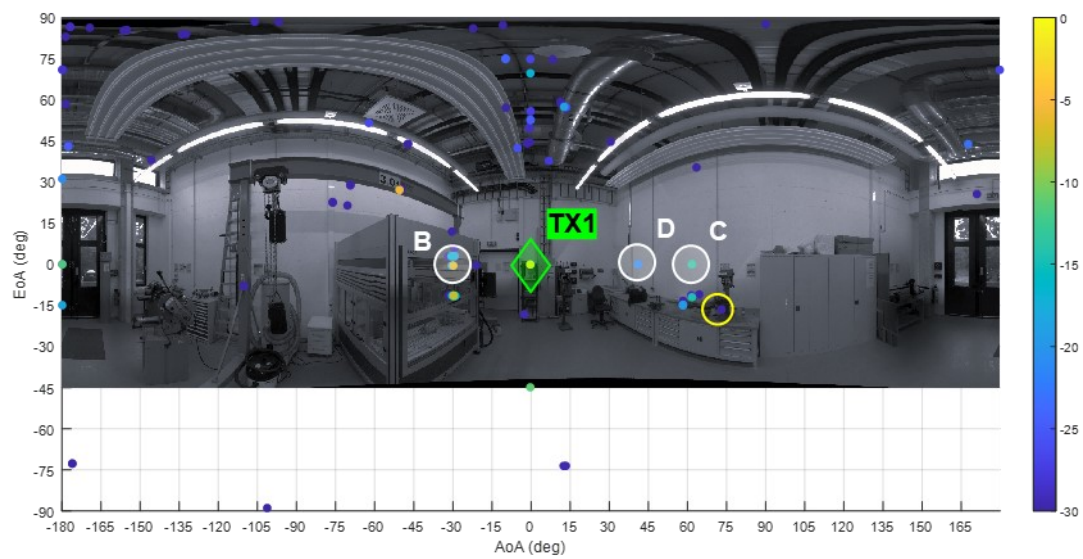
(b)

Figure 22: Underlaid picture and plain RT simulations in the machine room scenario in the LOS link TX1-RX1 from (a) TX view, and (b) RX view.

Similar results are observed in the NLOS simulations in Figure 23, where the reflections in the lightbulb holders and pipes in the ceiling are also observed together with the main reflections in the wall and metallic frames of the door at the end of the room in marked in white circles in Figure 23(a). In addition, the reflections in the clutter tools at 15° azimuth and -15°elevation of departure are also well captured by the RT tool, as seen in Figure 23(a).
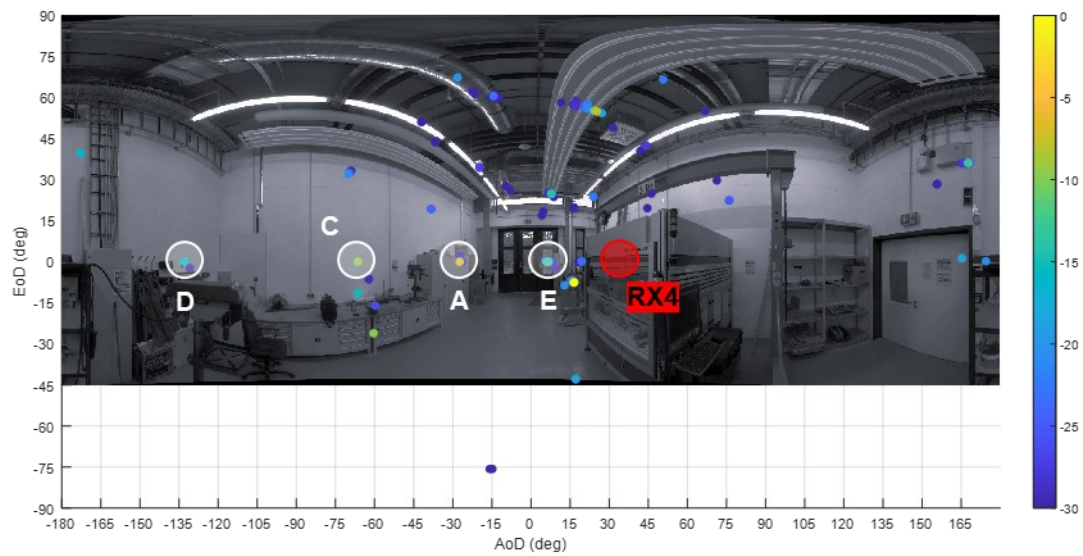
(a)
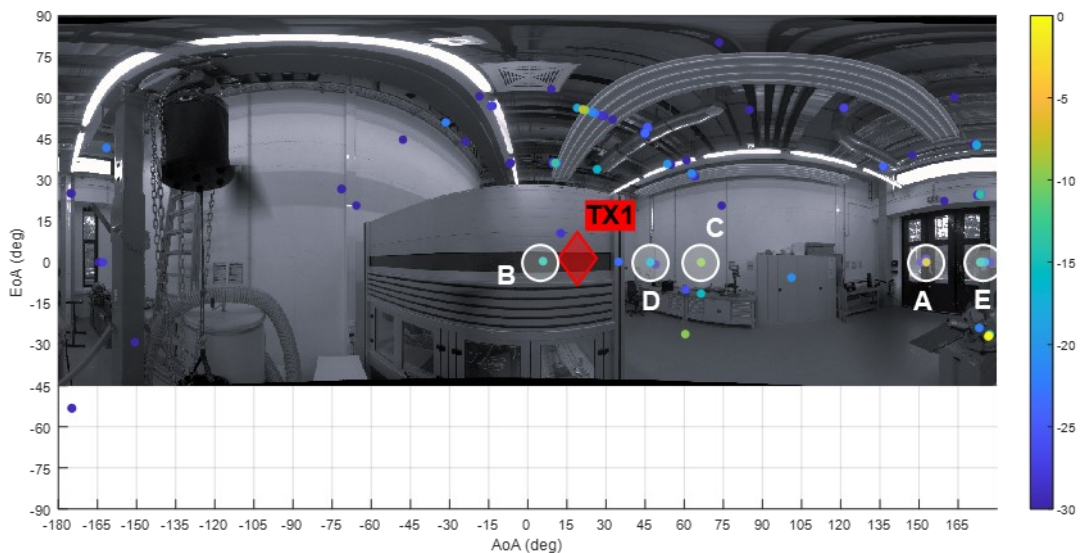
(b)

Figure 23: Underlaid picture and plain RT simulations in the machine room scenario in the NLOS link TX1-RX4 from (a) TX view, and (b) RX view.

5.3   Validation of the Deterministic Components from the RT Simulations with Multi-band Measurements in the Machine Room Scenario

The large industry hall model has been partially validated in the Deliverable D3.1 where it was introduced. More details can be found in [NDV22]. Therefore, we concentrate in the validation of the machine room scenario.

For the sake of simplicity, only two positions (one in LOS and in NLOS) will be analysed in detail. For consistency, we have chosen the same positions that were used to analyse propagation in the Deliverable 3.3 in the machine room scenario.

The multi-band RT simulated and measure PAAP for the LOS link TX1-RX1 are displayed in Figure 24. The effects of the wider antenna pattern at 6.75 GHz are observed in the more diffused pattern. The dominant clusters (A, B, C, and D) marked in Figure 22(a) are present both in the measurements and simulations. The path A is the LOS component, B is a single specular reflection in the milling machine, C is also a single specular reflection in the wall, and D is a double bounce reflection in the rear and side walls. The isotropic characteristic of the channel in LOS seems to be dominated by specular reflections on the macro-structure of the room/environment.
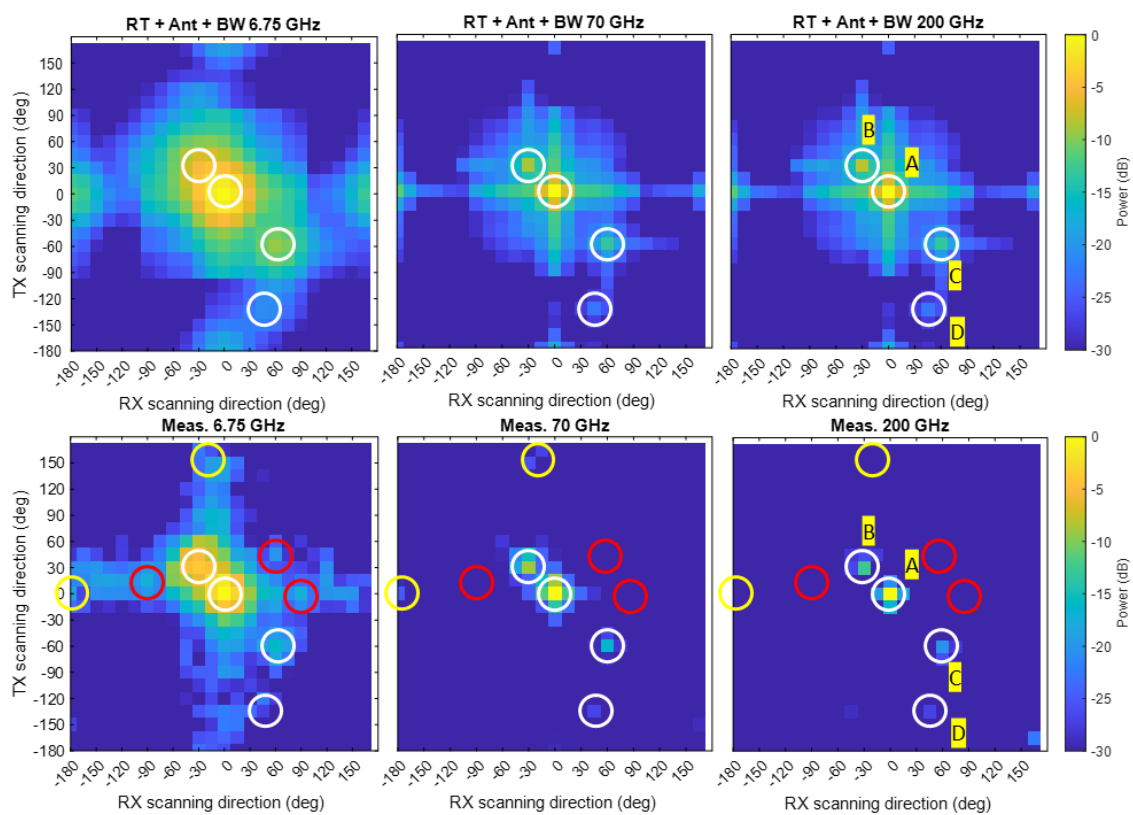
Figure 24: Measured and RT simulated multi-band PAAP for the LOS link TX1-RX1 in the machine room scenario.

Similarly, the NLOS link TX1-RX4 is analysed in Figure 25. Comparing to the picture and plain RT simulations in Figure 23(a) and (b), we can also observe a good match between the simulated and measured dominant components. In addition, there are strong components in the measurements that are not well captured by the simulations, as the one indicated in the red circle, which is visible at 6.75 GHz, but not at mmWave and (sub-)THz.

The RT simulations assisted on the interpretation of the measurement results. Scatterer D corresponds to the double reflection on the rear and side walls, marked as D as well in the LOS measurement. Scatterer A is a strong double reflection on the cupboards and frames of the

door. Scatterer E is a single reflection in the frames of the doors, and F is most probably from diffraction (it can also be observed a decaying path gain with increasing frequency). Finally, B is a high order reflection between the frames of the doors and the milling machine.
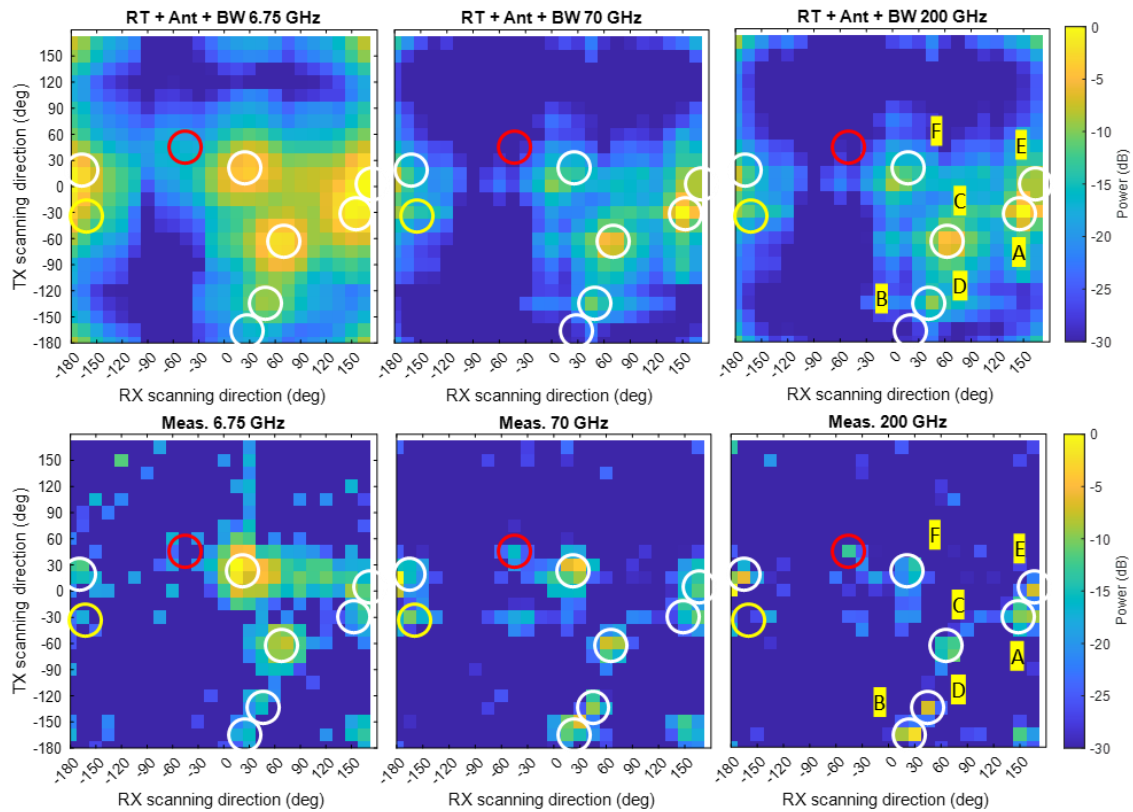
Figure 25: Measured and RT simulated multi-band PAAP for the NLOS link TX1-RX4 in the machine room scenario.

The analysis of polarization also showed a relatively good match where the RT was able to accurately predict the influence of polarization. The measured and RT simulated PAAP decomposed on their polarimetric components is displayed in Figure 26, where similarly to what was analysed in the Deliverable D3.4, we can observe that the reflection on the wall and machine (scatterer B and C) are stronger in the V-V polarization than in the H-H. The RT simulations represented the same case.
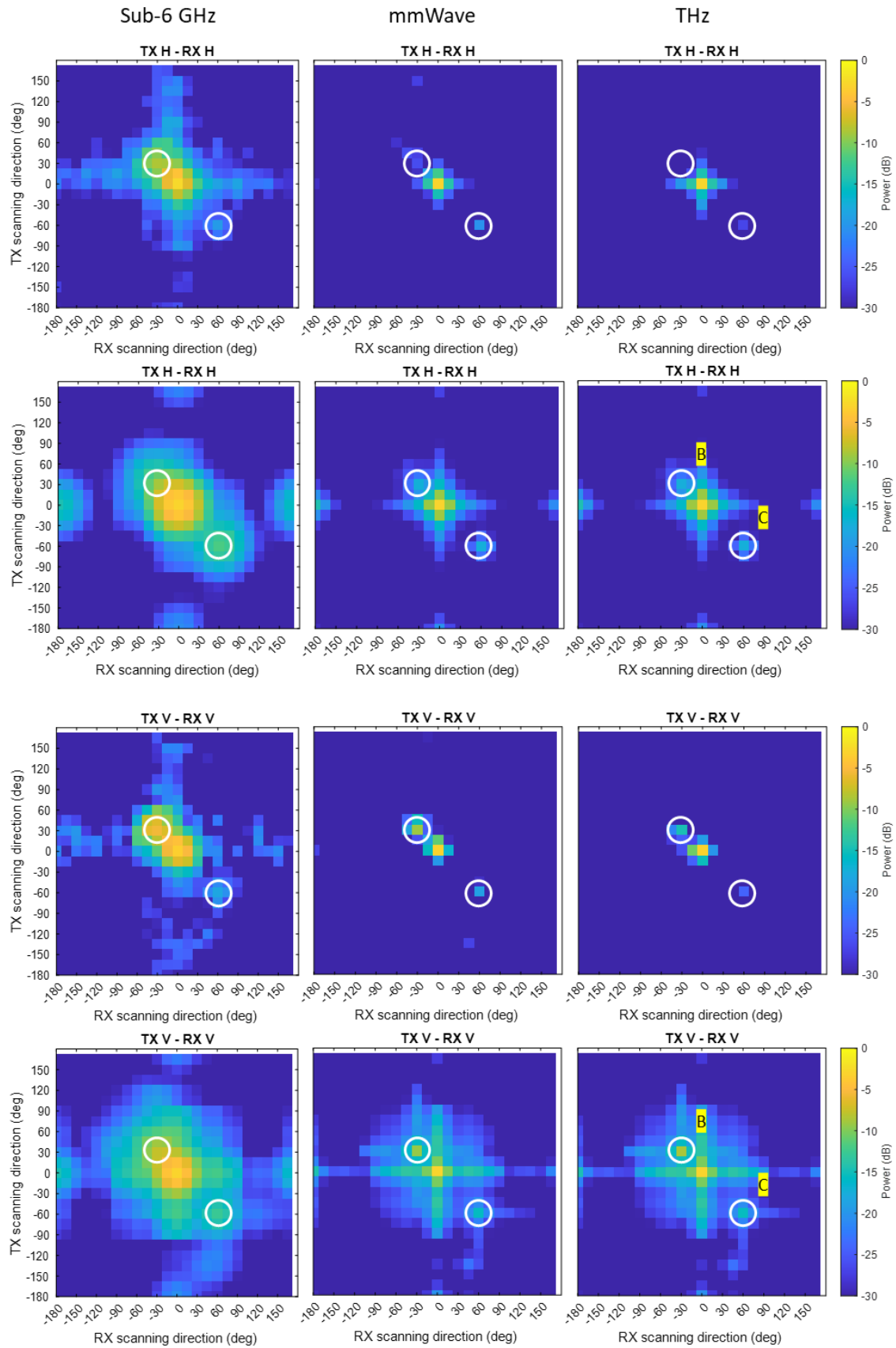
Figure 26: Measured and simulated polarimetric multi-band PAAP comparison in the LOS link TX1-RX1 in the machine room scenario.

The simulated and measured power azimuth/delay profile at the RX in the NLOS link TX1-RX4 is displayed in Figure 27, where most of the measured paths are observed in the simulations. However, there is a scatterer (marked in red) that in the measurements is highly attenuated at 200 GHz but in the simulations is still strong.
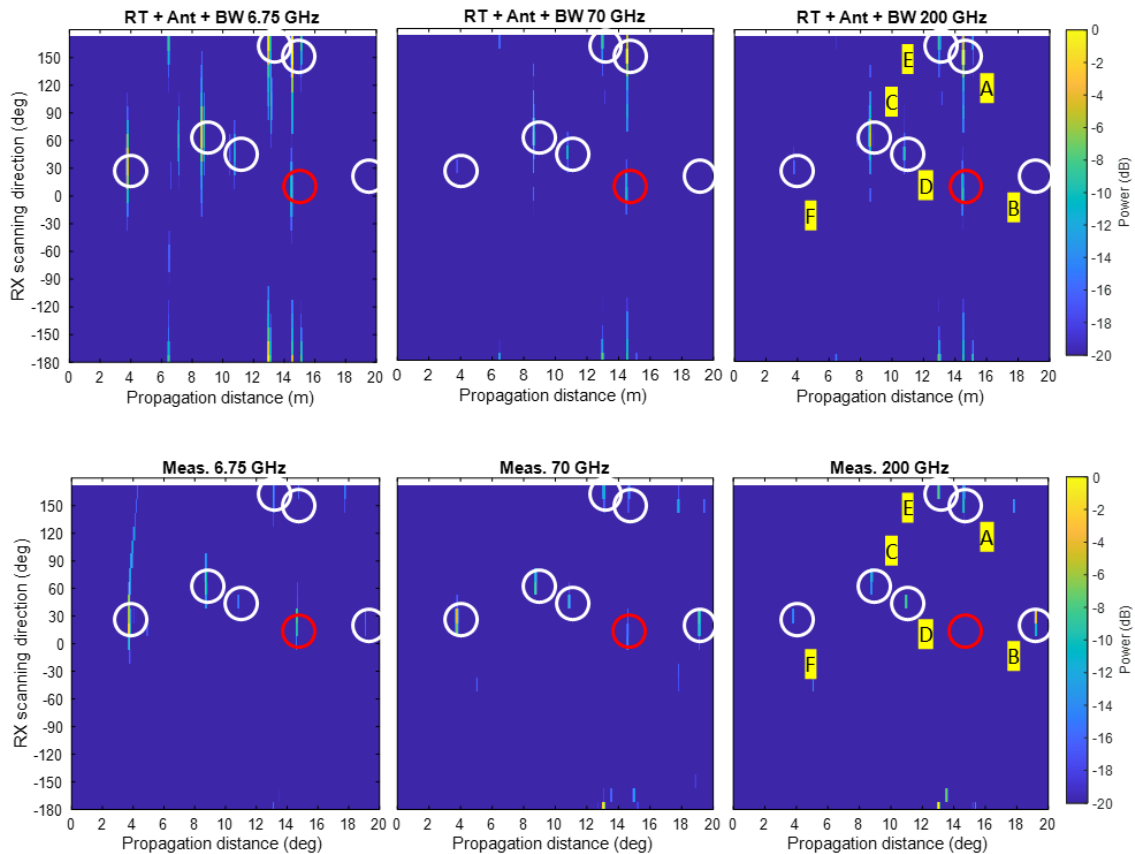
Figure 27: Measured and simulated PADP at the RX in the NLOS link TX1-RX4 in the machine room scenario.

Finally, the simulated and measured multi-band synthetic omni-directional PDP in the LOS link TX1-RX1 and NLOS link TX1-RX4 are displayed in Figure 28(a) and (b), respectively. The discrete nature of the simulations and the limited number of possible calculated MPCs can be observed in the result of a sparser PDP than the measured ones.

In the LOS case in Figure 28(a) we can observe that the RT simulates a set of strong MPCs around 5 and 6.5 m propagation distance that were not captured by the measurements. Many of them were simulated stronger at sub-6 GHz. A similar result was obtained in the NLOS case in Figure 28 (b), where there are also paths in the region of 5 to 7 m propagation distance that were not captured by the measurements. The origin will be further investigated and corrected.

In addition, we can observe a difference on the path gain between the paths found simultaneously in the measurements and simulations. The origin of this mismatch can be from multiple sources:

- Differences on the constructive materials between reality and model
- Differences on the electromagnetic properties of the materials
- Fading: in reality, there might be multiple closely located unresolved paths that generate fading within the measured channel tap considering the limited bandwidth
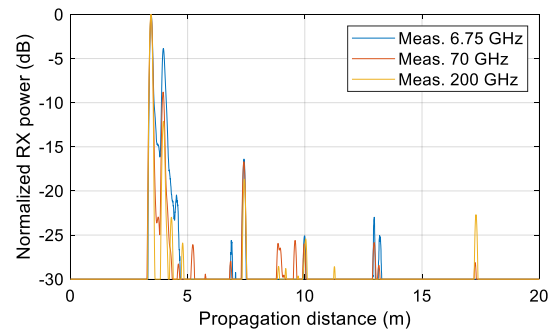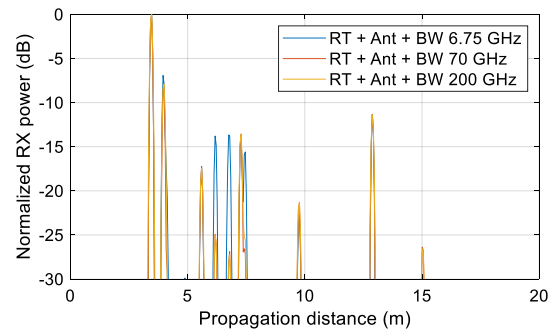
(a)
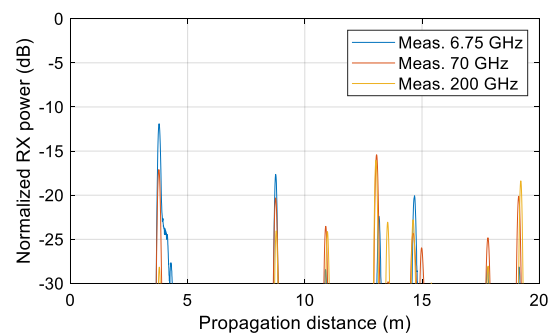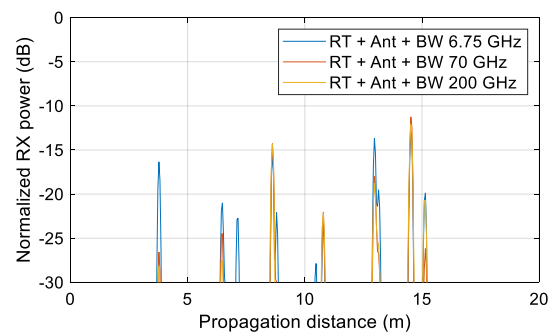
(b)

Figure 28: Measured and simulated multi-band PDP in the (a) LOS link TX1-RX1, and (b) NLOS link TX1-RX4.

5.4　Validation of the Large-Scale Parameters

The LSPs calculated from the RT simulations and measurements individually per link are summarized in the following figures. In general, a good agreement between the measured and simulated values of the LSPs are observed. The simulations also present a frequency dependence due to the different electromagnetic properties of the materials in the environment.
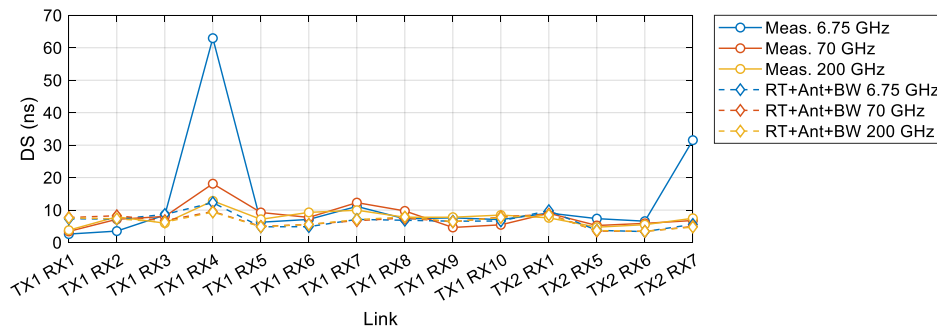
(a)
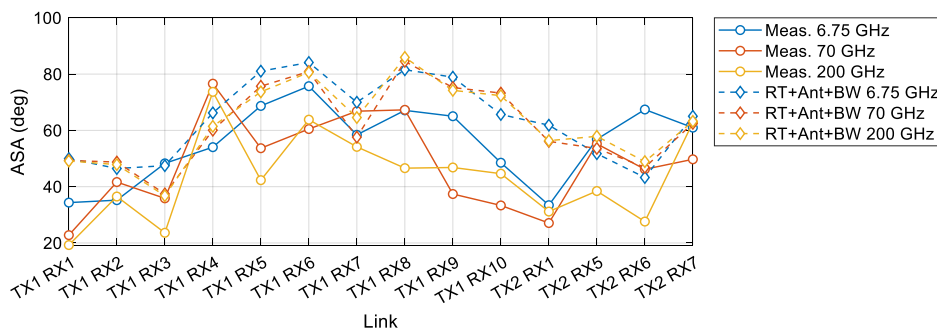
(b)
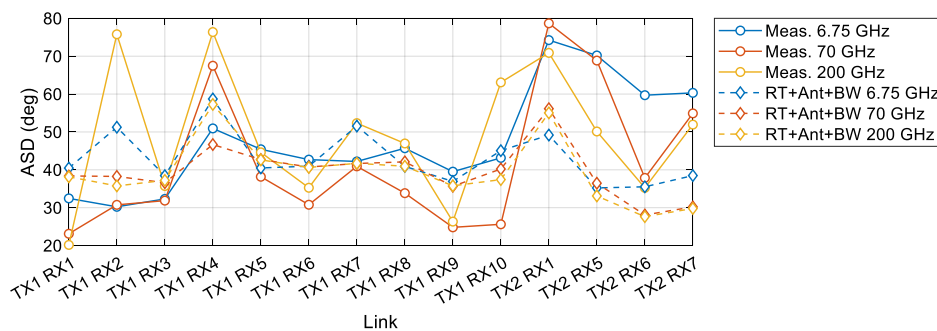
(c)
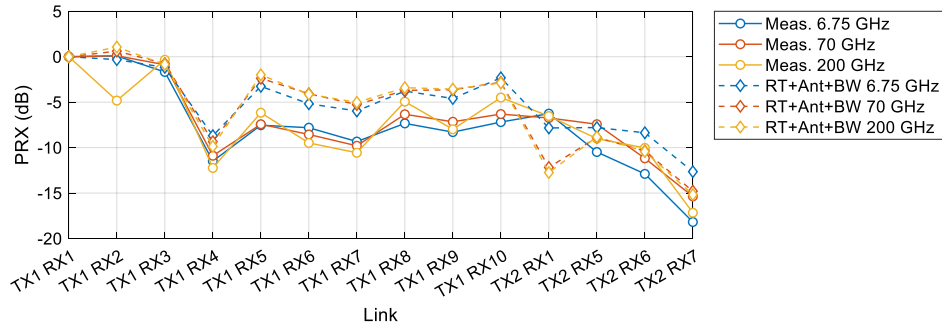
(d)
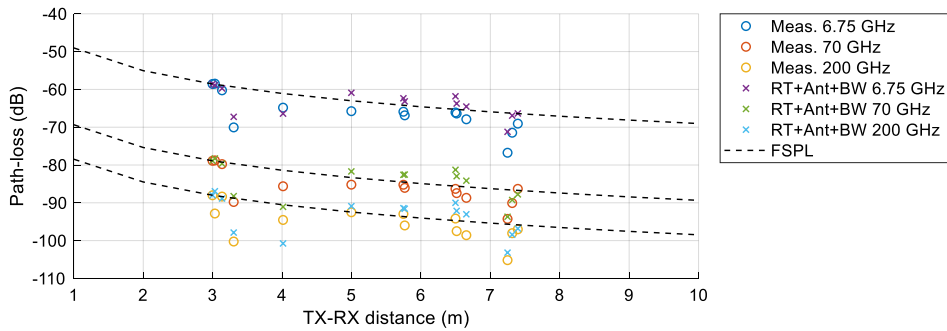
(e)

Figure 29: Per-link measured and simulated LSPs in the machine room scenario: (a) DS, (b) ASA, (c) ASD, (d) Received Power, and (e) Path-loss.

The cumulative distribution function of the LSPs separated in LOS and NLOS is presented in Figure 30 (a) and (b), respectively. There is not a clear relation between the LSPs and the frequency neither in the simulations nor in the measurements.
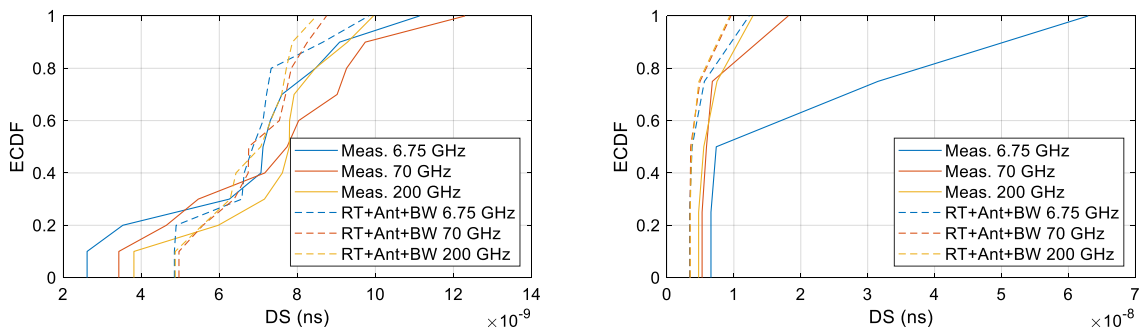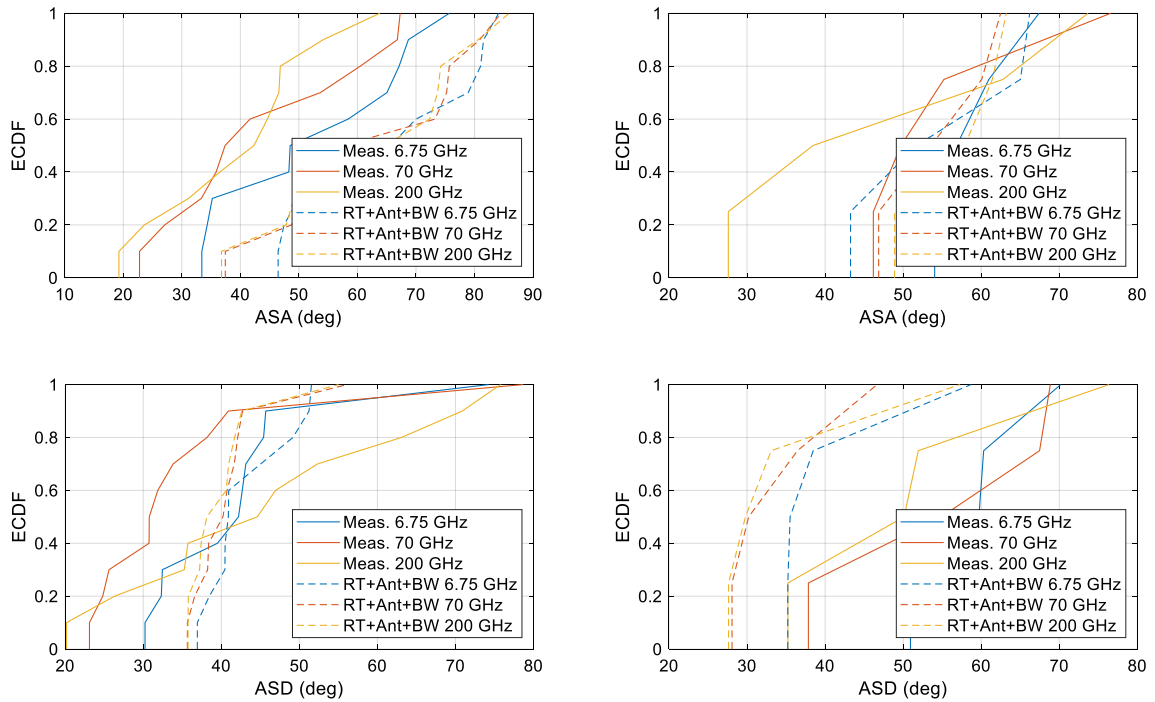
Figure 30: CDF of the LSPs separated in LOS (first column), and NLOS (second column).

It is worth to remember that these values correspond to the simulations considering the same set-up used during the measurements. These values are only used as a reference to validate the model. Once the model is contrasted with the measurements, simulations considering isotropic properties on the antennas can be conducted to estimate LSPs than can be used to generate statistics of the environment or for application specific simulations.

6   Validation of the RT Model of the Laboratory Scenario from Infrared-band Measurements

In an optical wireless communication (OWC) system, there are two types of light paths from the transmitter to the receiver. The dominant path in OWC is line-of-sight (LOS) from the light emitting diode (LED) to the receiver. The other paths come from reflections, namely non-LoS (NLOS). Although the LOS link dominates the channel propagation, NLOS link has a non-negligible effect, especially in the complex scenario with numerous reflectors [FYH18]. This can be verified from the practical measurement results of OWC channel on the production line in the Deliverable D3.3. Thus, a novel OWC channel modelling and channel characteristic analysis platform was jointly developed by Nanchang University (NCU) and Institut supérieur d'électronique de Paris (ISEP).
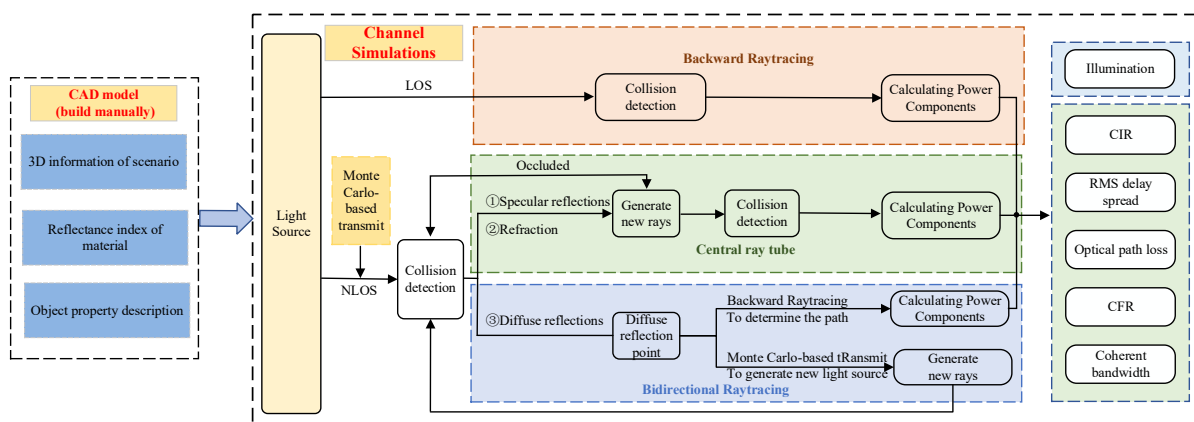
Figure 31: Structure of the proposed channel modelling and analysis platform

In the practical OWC channel modelling, various reflection and refraction problems may be encountered, this makes channel modelling more complex. A novel channel modelling and channel characteristic analysis platform, as shown in Figure 31, was proposed based on the bidirectional ray tracing method. Specifically, the proposed bidirectional ray tracing combines both bidirectional ray tracing and Monte Carlo ray launching techniques based on the central ray tube method. Firstly, to address the most common diffuse reflection challenges in channel modelling, we have devised a bidirectional ray tracing algorithm that enhances the accuracy of received power gain contributions from diffuse reflection paths and improves simulation efficiency. Secondly, to address specular reflection and refraction in channel modelling, we have designed a central ray tube model combined with a forward tracing algorithm based on the Monte Carlo ray launching method. This approach allows simultaneous simulation of specular reflection and refraction phenomena occurring at different medium surfaces, significantly enhancing computational efficiency and tracking precision. Based on the proposed structure, we can obtain the direct, reflected, and refracted path components in terms of received power and optical path length at the receiver, thereby enabling the computation of channel impulse response and other illumination and communication performance metrics.

In order to verify the effectiveness of the proposed channel modelling and analysis platform, the channel spatial properties are compared between the channel platform-based simulated and measured OWC channel data. For the sake of simplicity, only the exchange discussion area located in the centre of the laboratory (as shown in Figure 9) is analysed in detail.
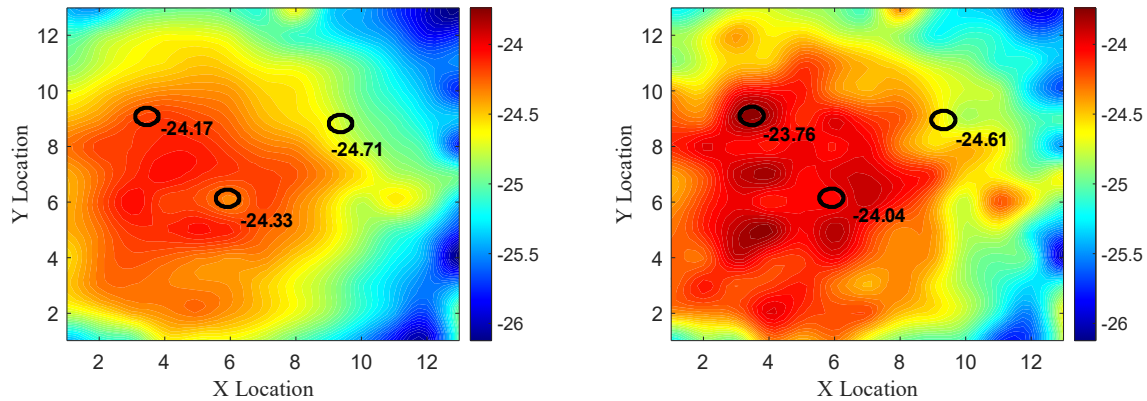
Figure 32: Spatial properties of simulated and measured OWC channel in the laboratory scenario.

It can be seen from Figure 32 that the channel gain distribution achieved by the channel modelling and analysis platform is close to the practical analyzed data from the measured data. Specifically, we randomly select three channel gain at the same position in the channel gain distribution figure. The difference between the simulated and the measured data is optimistic and controllable. The reason for this difference comes from two aspects. On the one hand, there are still errors between the 3D model obtained through scanning software and the practical 3D scenario. On the other hand, in order to balance calculation accuracy and efficiency, the limited number of reflection units and the number of bounces have to be considered during the simulation calculation process.

7 Summary and Concluding Remarks

In this deliverable we have presented the physical channel modelling methodology to address multi-band systems in industrial environments. The presented model is a deterministic/stochastic model based on precise RT simulations from realistic maps of scenarios obtained from LiDAR measurements. The different objects in the environment are parametrized with electromagnetic properties to re-create frequency dependent CIRs. The core of the simulations are the results of the RT process. They are later combined with stochastic components generated with two purposes: introduce small variations in the environment (in case there is not a scenario specific need on the simulations) and to compensate missing components that are not generated with the RT simulations. In addition, events as shadowing are also generated randomly to recreate possible obstruction events during communications.

The map of the RT model and the results of the RT simulations have been validated with multi-band measurements conducted in the same scenario. The analysis of individual marginal power profiles has shown large similarities in LOS and NLOS situations. However, small differences arise since the RT map is a discrete representation of the environment. Therefore, some MPCs are not present (from objects that were not included in the map), and some extra MPCs are created during simulations from facets of objects that in the simulations are created with polygons, but in reality, the surface is smoother. However, even considering these small differences, the main components have been successfully recreated.

The geometrical properties of the MPCs have matched very well the ones observed in the measurements. In addition, polarization also has been analysed with positive results, in which the influence of the polarization was observed in the amplitude of the reflected paths in the walls and frames of the machine.

This model has been used to support further investigations on system deployment within 6G BRAINS. As a result, the model can be used purely deterministic based on the maps (BOSCH factory in Blaichach and machine room in FhG, Ilmenau), or with the stochastic features, accordingly to the simulation requirements.

Future tasks are to enrich the model with more details and continue adjusting the material properties to obtain stronger similarities with the measurements in terms of amplitude of the MPCs. In addition, there are multiple modelling aspects to be improved:

- Displacement at high frequencies: life span of the MPCs.
- Blockage loss at different frequencies: moving objects in the environment not only block the LOS, but also different MPCs. However, this blockage loss depends on the frequency, and while the event of blockage (duration and number of MPCs) is the same for co-located radio-interfaces, the attenuation depends on the band.
- Angular description of the DMCs: so far in this implementation, the analysis of the DMC was performed over the synthetic omni-directional PDP and the DMCs were calculated with uniform angular distribution. However, there is a spatial relation on the concentration of DMC.

Furthermore, the geometrical information obtained from the RT simulations will be used to integrate the modelling parameters extracted from the OWC measurements in Deliverable D3.3 to obtain a deterministic/stochastic model covering also this band.

References

[3GP20]   3GPP , **"TR 38.90: Study on channel model for frequencies from 0.5 to 100 GHz,"** 2020.

[ACC22a]   Mohamed Aliouane, Jean-Marc Conrat, Jean-Christophe Cousin, and Xavier Begaud, **"Indoor Material Transmission Measurements between 2 GHz and 170 GHz for 6G Wireless Communication Systems,"** in 2nd Technical Meeting COST CA20120 INTERACT, Lyon, France, June 13-15, 2022.

[ACC22b]   Mohamed Aliouane, Jean-Marc Conrat, Jean-Christophe Cousin, and Xavier Begaud, **"Material Reflection Measurements in Centimeter and Millimeter Wave ranges for 6G Wireless Communications,"** in 2nd Technical Meeting COST CA20120 INTERACT, Lyon, France, June 13-15, 2022.

[AJ07]   S. Arumugam, and J. John, "**Effect of transmitter positions on received power and bandwidth in diffuse indoor optical wireless systems**," Optical and Quantum Electronics, vol. 39, no. 1, Apr. 2007, pp. 1–14.

[AWH16]   A. Al-Kinani, C.-X. Wang, H. Haas, and Y. Yang, "**Characterization and modeling of visible light communication channels**," in 2016 IEEE Vehicular Technology Conference - Spring, Nanjing, China, May 2016, pp. 1–5.

[AWZ18]   A. Al-Kinani, C. -X. Wang, L. Zhou, and W. Zhang, "**Optical Wireless Communication Channel Measurements and Models**," IEEE Communications Surveys & Tutorials, vol. 20, no. 3, pp. 1939-1962, thirdquarter 2018.

[BCA17]   A. Behlouli, P. Combeau, and L. Aveneau, "**MCMC Methods for Realistic Indoor Wireless Optical Channels Simulation**," Journal of Lightwave Technology, vol. 35, no. 9, pp. 1575-1587, 1 May1, 2017.

[BKK93]   J. R. Barry, J. M. Kahn, W. J. Krause, E. A. Lee, and D. G. Messerschmitt, "**Simulation of multipath impulse response for indoor wireless optical channels**," IEEE Journal on Selected Areas in Communications, vol. 11, no. 3, pp. 367–379, Apr. 1993.

[CBH16]   C. Chen, D. Basnayaka, and H. Haas, "**Non-line-of-sight channel impulse response characterisation in visible light communications**," in 2016 IEEE International Conference on Communications (ICC), Kuala Lumpur, Malaysia, 2016, pp. 1-6.

[CC05]   J. B. Carruthers and S. M. Carroll, "**Statistical impulse response models for indoor optical wireless channels**," International Journal of Communication Systems, vol. 18, no. 3, pp. 267–284, Apr. 2005.

[CJJ20]   P. Combeau, S. Joumessi-Demeffo, A. Julien-Vergonjanne, L. Aveneau, S. Sahuguède, H. Boeglen, and D. Sauveron, "**Optical Wireless Channel Simulation for Communications Inside Aircraft Cockpits**," Journal of Lightwave Technology, vol. 38, no. 20, pp. 5635-5648, 15 Oct.15, 2020.

[CK02]   J. B. Carruthers and P. Kannan, "**Iterative site-based modeling for wireless infrared channels**," IEEE Transactions on Antennas and Propagation, vol. 50, no. 5, pp. 759–765, May 2002.

[CK97]   J. B. Carruthers and J. M. Kahn, "**Modeling of nondirected wireless infrared channels**," IEEE Transactions on Communications, vol. 45, no. 10, pp. 1260–1268, Oct. 1997.

[CZK14]   M. I. S. Chowdhury, W. Zhang, and M. Kavehrad, "**Combined Deterministic and Modified Monte Carlo Method for Calculating Impulse Responses of Indoor Optical Wireless Channels**," Journal of Lightwave Technology, vol. 32, no. 18, pp. 3132-3148, Sept. 2014.

[DAS21]   D. Dupleich, H. Abbas Mir, C. Schneider, G. Del Galdo and R. Thomä, "**On the Modelling of the NLOS First Multi-path Component in Stochastic Spatial Channel Models**," 2021 15th European Conference on Antennas and Propagation (EuCAP), 2021, pp. 1-5.

[DFV07]   V. Degli-Esposti, F. Fuschini, E. M. Vitucci and G. Falciasecca, "**Measurements and Modelling of Scattering from Buildings**," IEEE Transactions on Antennas and Propagation, 2007.

[DML20]   D. Dupleich, R. Müller, M. Landmann, J. Luo, G. Del Galdo and R. S. Thomä, "**Multi-band Characterization of Propagation in Industry Scenarios**," in *14th European Conference on Antennas and Propagation (EuCAP)*, Copenhagen, Denmark, 2020, pp. 1-5.

[FYH18]   L. Feng, H. Yang, R. Q. Hu and J. Wang, "**MmWave and VLC-based indoor channel models in 5G wireless networks**," in IEEE Wireless Communications, vol. 25, no. 5, pp. 70-77, October 2018.

[GB79]   F. R. Gfeller and U. Bapst, "**Wireless in-house data communication via diffuse infrared radiation**," Proceedings of the IEEE, vol. 67, no. 11, pp. 1474-1486, Nov. 1979.

[HI07]   N. Hayasaka and T. Ito, "**Channel modeling of nondirected wireless infrared indoor diffuse link**," Electronics and Communications in Japan (Part I: Communications), vol. 90, no. 6, pp. 10–19, 2007.

[JNH02]   V. Jungnickel, V. Pohl, S. Nonnig, and C. V. Helmolt, "**A physical model of the wireless infrared communication channel**," IEEE Journal on Selected Areas in Communications, vol. 20, no. 3, pp. 631–640, Apr. 2002.

[KB97]   J. M. Kahn and J. R. Barry, "**Wireless infrared communications**," Proceedings of the IEEE, vol. 85, no. 2, pp. 265–298, Feb. 1997.

[LEE09]   H. S. Lee, "**A Photon Modeling Method for the Characterization of Indoor Optical Wireless Communication**", Progress In Electromagnetics Research, vol. 92, pp. 121–136, 2009.

[LHB97]   F. J. López-Hernández and M. J. Betancor, "**DUSTIN: Algorithm for calculation of impulse response on IR wireless indoor channels**," Electronics Letters, vol. 33, no. 21, pp. 1804–1806, Oct. 1997.

[LPB11]   K. Lee, H. Park, and J. R. Barry, "**Indoor channel characteristics for visible light communications**," IEEE Communications Letters, vol. 15, no. 2, pp. 217–219, Feb. 2011.

[LPS98a]   F. J. López-Hernández, R. Pérez-Jiménez, and A. Santamaria, "**Monte Carlo calculation of impulse response on diffuse IR wireless indoor channels**," Electronics Letters, vol. 34, no. 12, pp. 1260–1262, Jun. 1998.

[LPS98b]   F. J. López-Hernández, R. Pérez-Jiménez, and A. Santamaria, "**Modified Monte Carlo scheme for high-efficiency simulation of the impulse response on diffuse IR wireless indoor channels**," Electronics Letters, vol. 34, no. 19, pp. 1819–1820, Sep. 1998.

[ITU21]   Reccomendation ITU-R P.2040-2, **"Effects of building materials and structures on radiowave propagation above about 100 MHz,"** Online: https://www.itu.int/dms_pubrec/itu-r/rec/p/R-REC-P.2040-2-202109-I!!PDF-E.pdf

[LFR96]   O. Landron, M. J. Feuerstein and T. S. Rappaport, **"A comparison of theoretical and empirical reflection coefficients for typical exterior wall surfaces in a mobile radio environment"**, IEEE Transactions on Antennas and Propagation, vol. 44, no. 3, pp. 341-351, 1996.

[MET15]   **"Deliverable D1.4: METIS Channel Models,"** 2015.

[MGK22]   S. M. Mana, K. G. K. Gabra, S. M. Kouhini, M. Hinrichs, D. Schulz, P. Hellwig, A. Paraskevopoulos, R. Freund, and V. Jungnickel, "**LIDAR-Assisted Channel Modelling for LiFi in Realistic Indoor Scenarios**," IEEE Access, vol. 10, pp. 59383-59399, 2022.

[MU15]   F. Miramirkhani and M. Uysal, "**Channel modeling and characterization for visible light communications**," IEEE Photonics Journal, vol. 7, no. 6, pp. 1–16, Dec. 2015.

[PBB97]   R. Pérez-Jiménez, J. Berges, and M. J. Betancor, "**Statistical model for the impulse response on infrared indoor diffuse channels**," Electronics Letters, vol. 33, no. 15, July 1997, pp. 1298–1300.

[NDV22]   H. Niu et al., **"From 3D Point Cloud Data to Ray-tracing Multi-band Simulations in Industrial Scenario,"** 2022 IEEE 95th Vehicular Technology Conference: (VTC2022-Spring), 2022, pp. 1-5.

[PK13]   S. Priebe and T. Kurner, **"Stochastic Modeling of THz Indoor Radio Channels,"** in IEEE Transactions on Wireless Communications, vol. 12, no. 9, pp. 4445-4455, September 2013.

[PKJ13]   S. Priebe, M. Kannicht, M. Jacob and T. Kürner, **"Ultra broadband indoor channel measurements and calibrated ray tracing propagation modeling at THz frequencies,"** in Journal of Communications and Networks, vol. 15, no. 6, pp. 547-558, Dec. 2013

[PJ00]   R. Pérez-Jiménez, "**Ray-tracing algorithms for fast calculation of the channel impulse response on diffuse IR wireless indoor channels**," Optical Engineering, vol. 39, no. 10, pp. 2775, Oct. 2000.

[PJK11]   S. Priebe, M. Jacob and T. Kuerner, **"AoA, AoD and ToA Characteristics of Scattered Multipath Clusters for THz Indoor Channel Modeling,"** 17th European Wireless 2011 - Sustainable Wireless Technologies, 2011, pp. 1-9.

[PSD11]   J. Poutanen, J. Salmi, K. Haneda, V. -M. Kolmonen and P. Vainikainen, **"Angular and Shadowing Characteristics of Dense Multipath Components in Indoor Radio Channels,"** in IEEE Transactions on Antennas and Propagation, vol. 59, no. 1, pp. 245-253, Jan. 2011

[PSH10]   J. Poutanen, J. Salmi, K. Haneda, V. -M. Kolmonen, F. Tufvesson and P. Vainikainen, **"Propagation Characteristics of Dense Multipath Components,"** in IEEE Antennas and Wireless Propagation Letters, vol. 9, pp. 791-794, 2010.

[RPL02]   S. Rodríguez-Pérez, R. Pérez-Jiménez, F. J. López-Hernández, O. B. González-Hernández, and A. J. Ayala-Alfonso, "**Reflection model for calculation of the impulse response on IR-wireless indoor channels using ray-tracing algorithm**," Microwave and Optical Technology Letters, vol. 32, no. 4, pp. 296–300, Jan. 2002.

[RPR13]   S. Rodríguez-Pérez, R. Pérez-Jiménez, B. Rodriguez-Mendoza, F. J. López-Hernández, and A. J. Ayala-Alfonso, "**Simulation of impulse response for indoor visible light communications using 3D CAD models**," EURASIP Journal on Wireless Communications and Networking, vol. 2013, no. 1, Jan. 2013.

[SCH16]   H. Schulze, "**Frequency-Domain Simulation of the Indoor Wireless Optical Communication Channel**," IEEE Transactions on Communications, vol. 64, no. 6, pp. 2551-2562, June 2016.

[SUA14]   E. Sarbazi, M. Uysal, M. Abdallah, and K. Qaraqe, "**Indoor channel modelling and characterization for visible light communications**," in 2014 International Conference on Transparent Optical Networks (ICTON), Graz, Austria, Jul. 2014, pp. 1–4.

[WPK16]   R. J. Weiler, M. Peter, W. Keusgen, A. Maltsev, A. P. I. Karls, I. Bolotin, I. Siaud and A. M. Ulmer-Moll, **"Quasi-deterministic millimeter-wave channel models in MiWEBA,"** EURASIP, 2016.

[YH22]   A. Yesilkaya and H. Haas, "**Channel Modelling and Error Performance Investigation for Reading Lights Based In-Flight LiFi**," IEEE Transactions on Vehicular Technology, vol. 71, no. 5, pp. 4949-4964, May 2022.

[ZWH22]   X. Zhu, C. -X. Wang, J. Huang, M. Chen, and H. Haas, "**A Novel 3D Non-Stationary Channel Model for 6G Indoor Visible Light Communication Systems**," IEEE Transactions on Wireless Communications, vol. 21, no. 10, pp. 8292-8307, Oct. 2022.

[end of document]